

Effects of smooth flows on tracer gradients and tracer spectra

Valentin Resseguier, Bertrand Chapron, Etienne Mémin

June 15, 2017

Abstract

During a finite-time advection, the norm of tracer gradients can increase or decrease, depending on the angle between flow gradients and initial tracer gradients. When the correlation between these two fields is weak – either because the tracer has a negligible back effect on the flow or because a strong spatial smoothing has been performed – the averaged squared norm of tracer gradients can only increase. Moreover, the local growth rate of the tracer gradients is independent of the initial tracer distribution. As presented, this growth rate is directly related to FTLE and mesochronic velocity. A simple model is then proposed to locally and globally describe the time evolution of the growth rate in the case of a stationary or slowly time evolving Eulerian velocity field. The key processes are locally uniform shears and foldings around stationary vortices. Finally, the squared norm mean of tracer gradients controls and specifies the time evolution of the spectral tail and its slope. Accordingly, the advection time and low-pass filter width can be determined for practical applications using a Lagrangian advection method. This analysis suggests a practical eddy diffusivity parameterization. Numerical experiments on a toy model and using satellite data illustrate these developments.

1 Introduction

Since the first images from space, the attention of both theoreticians and remote sensing scientists has been triggered by the abundance of various ocean tracer patterns and signatures in the mesoscale and submesoscale (1-50 km) ranges (e.g. Gower et al., 1980; Lesieur and Sardouny, 1981). To date, global direct quantification of horizontal dispersion and mixing at such scales is still not available. Yet, from precise measurements of the ocean topography and its related dynamics, significant progress has been made. Nowadays, combined satellite altimeter measurements satisfactorily detail the large scale ocean dynamics. The ocean’s mesoscale (10-50 km) and submesoscale (< 10 km) variability and energy are still more challenging to map with conventional radar altimeters, mainly because of the narrow illuminated swath of each instrument, regardless of the orbital configuration (Dufau et al., 2016).

Nonetheless, a now-common strategy is to derive small-scale tracer structures and so-called Lagrangian co-

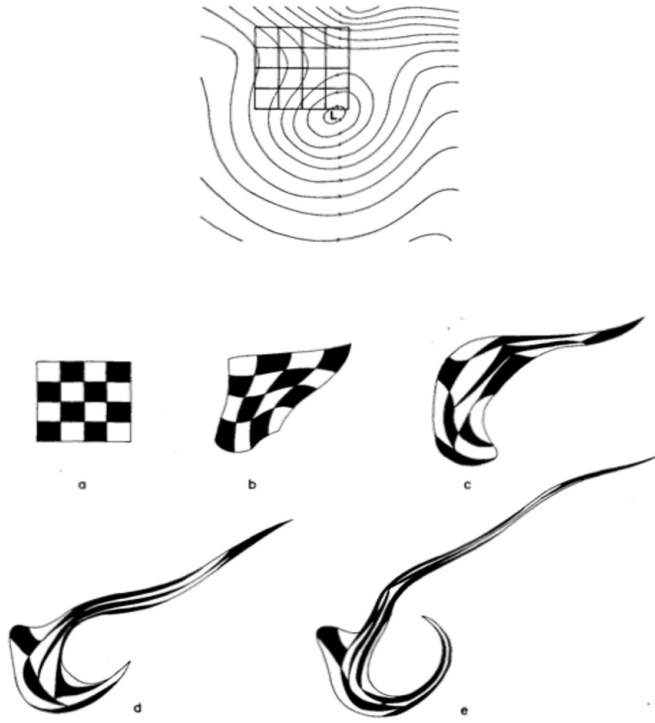


Figure 1: Deformation of an air layer in the atmosphere after 6 hours, 12 hours, 24 hours and 36 hours respectively. A simple barotropic model is used to simulate the flow (Welander, 1955).

herent structures, from the available smooth altimetry-derived velocities (e.g. Price et al., 2006; Lehahn et al., 2007). Indeed, using a Lagrangian-dynamical framework, an initial larger-scale tracer field can be advected on higher-resolution grids, generating much smaller-scale patterns (Aref, 1984; Pierrehumbert and Yang, 1993). Typical moderate- to large-scale ocean cyclonic and anti-cyclonic eddies trap and advect fluid parcels over weeks to months. As pictured, with time, these fluid parcels with different origins, temperature, salinity and possibly different biogeochemical properties and/or contaminant loadings, come closer, to sharpen fronts but also to possibly dilute their properties, and promote transformative chemical reactions. To help trigger these processes, stirring effect first characterizes the development of elongated structures, well illustrated by Welander (1955), using a simple velocity field to produce spectacular distortions, Figure 1. Initial square elements, small compared to the length scale of the deforming flow field, become subject to translation, rotation and shearing. With time, deformation is significant. Increasingly long and thin filaments wrap around the eddy, and possibly fold. Folds then appear where the velocity gradient is perpendicular to the stream direction. Accordingly, at a given scale of observations, mixing can be associated with processes that act to minimize filament thinning and dilute sharp differences (gradients).

After a long advection by a smooth and slowly-varying velocity, the expected growth of passive tracer gradients can be theoretically obtained, as well as its related spectral tail evolution. From this analysis, local and global diagnoses of stretching and folding can further be developed. From a practical point of view, using estimated velocities from altimeter-derived sea surface height (SSH) measurements, the initial tracer

field, sea surface temperature (SST) or salinity (SSS), must thus be low-pass filtered prior to Lagrangian-advection operations. It can then be expected that the time of advection and the low-pass filter bandwidth are directly linked. Following the proposed development, an exact relation can indeed be determined. Such an analysis then provides a rigorous explanation to the heuristic choices used in Dencausse et al. (2014). This can further be compared to values that can be inferred from the knowledge of the Rossby deformation radius or the mean squared vorticity (Berti and Lapeyre, 2014).

The section 2 describes the tracer gradients after a finite-time advection, and the associated stretching and folding diagnoses. In section 3, the averaged tracer gradient norm is shown to control the tracer spectrum tail. Tools are provided to monitor the aforementioned Lagrangian advection method. Based on the proposed developments, section 4 rapidly discusses subgrid parametrizations of large-scale flow simulations.

2 Time evolution for the tracer gradient norm

In this section, we propose exact and approximate results to describe the mean of the gradient squared norm of an advected tracer T :

$$\overline{\|\nabla T\|^2}, \quad (2.1)$$

where the averaging operator $\overline{\bullet}$ is defined for every function f as follows:

$$\overline{f} = \frac{1}{S} \mathbb{E} \int_{\Omega} f, \quad (2.2)$$

$\Omega \subset \mathbb{R}^2$ is the spatial domain and $S < \infty$ its area. Even though we will mainly focus on deterministic dynamics, the expectation, \mathbb{E} , of the above formula enables us to directly generalize our results to random cases.

2.1 Exact flow properties

Given a possibly random velocity field \mathbf{v} , the flow $\mathbf{x}_0 \mapsto \phi(\mathbf{x}_0)$ is defined as:

$$\phi(\mathbf{x}_0) = \phi(\mathbf{x}_0, t) = \mathbf{x}_0 + \int_0^t dt' \mathbf{v}(\phi(\mathbf{x}_0, t'), t'). \quad (2.3)$$

For a divergence-free velocity, $\nabla \cdot \mathbf{v} = 0$, we have $\det(\nabla \phi^T) = 1$, where $\nabla \phi^T$ is the spatial gradient tensor of the flow. Subsequently, the right Cauchy-Green deformation tensor, $\nabla \phi^T (\nabla \phi^T)^T$, and its inverse, shall have two real and identical strictly positive eigenvalues. Only the stable direction, corresponding to the eigenvector associated with the eigenvalue smaller than 1, and the unstable direction, corresponding to the eigenvector associated with the eigenvalue larger than 1, are switched. Along the stable (resp. unstable) direction, the distance between two points decreases (resp. increases). More precisely, a matrix diagonalization

leads to:

$$\nabla\phi^T \left(\nabla\phi^T \right)^T = \mathbf{P}^T \mathbf{D}^{-1} \mathbf{P} \quad \text{with} \quad D_{ii}^{-1} = 1 + \alpha^2 \left(1 - (-1)^i \frac{\beta}{\alpha} \right), \quad (2.4)$$

where \mathbf{P} is an orthogonal matrix, $\alpha^2(\mathbf{x}_0) = \frac{1}{2} \|\nabla\phi^T\|^2 - 1 \geq 0$ and $\beta^2(\mathbf{x}_0) = \alpha^2 + 2$, using the Frobenius matrix norm. The eigenvalues D_{ii} define the Finite Time Lyapunov Exponents (FTLE) (Pierrehumbert and Yang, 1993; Haller and Yuan, 2000; Thiffeault and Boozer, 2001; Haller, 2005; Haller and Sapsis, 2011). The largest and the smallest FTLEs are:

$$\Lambda = \frac{1}{2t} \log(D_{11}^{-1}) \quad \text{and} \quad -\Lambda = \frac{1}{2t} \log(D_{22}^{-1}). \quad (2.5)$$

In particular, when both the largest FTLE, Λ , and the time, t , are large, the term α^2 is large and $\beta/\alpha = \sqrt{1 + \frac{2}{\alpha^2}}$ is small. This leads to the approximation:

$$\Lambda \approx \frac{1}{t} \log(\alpha), \quad (2.6)$$

Therefore, the FTLE ridges – often considered as proxies of mixing barriers – coincide with the α ridges. The Cauchy-Green tensor encodes insightful information on the flow. For instance, it rules the tracer gradient norm evolution. Noting that at a given time, the transported tracer gradient, ∇T , can be written from the initial gradient field, ∇T_0 , as:

$$\nabla T(\mathbf{x}) = \nabla(T_0(\phi^{-1}(\mathbf{x}))) = [\nabla\phi^T]^{-1}(\phi^{-1}(\mathbf{x})) \nabla T_0(\phi^{-1}(\mathbf{x})). \quad (2.7)$$

Then, using incompressibility in the variable change and the matrix diagonalization (2.4), we get an exact expression of the averaged squared norm of tracer gradients:

$$\overline{\|\nabla T\|^2} - \overline{\|\nabla T_0\|^2} = \frac{1}{S} \mathbb{E} \int_{\Omega} d\mathbf{x} \|\nabla T(\mathbf{x})\|^2 - \frac{1}{S} \mathbb{E} \int_{\Omega} d\mathbf{x}_0 \|\nabla T_0(\mathbf{x}_0)\|^2, \quad (2.8)$$

$$= \frac{1}{S} \mathbb{E} \int_{\Omega} d\mathbf{x}_0 \left\| [\nabla\phi^T]^{-1}(\mathbf{x}_0) \nabla T_0(\mathbf{x}_0) \right\|^2 - \frac{1}{S} \mathbb{E} \int_{\Omega} d\mathbf{x}_0 \|\nabla T_0(\mathbf{x}_0)\|^2, \quad (2.9)$$

$$= \overline{(\nabla T_0)^T \left([\nabla\phi^T (\nabla\phi^T)^T]^{-1} - \mathbb{I}_d \right) \nabla T_0}, \quad (2.10)$$

$$= \overline{\alpha^2 \left(\underbrace{\left(1 + \frac{\beta}{\alpha} \right)}_{>0} \left(\mathbf{P}^T \nabla T_0 \right)_2^2 + \underbrace{\left(1 - \frac{\beta}{\alpha} \right)}_{<0} \left(\mathbf{P}^T \nabla T_0 \right)_1^2 \right)}, \quad (2.11)$$

where $(\mathbf{P}^T \nabla T_0)_i$ is the i -th component of the vector $\mathbf{P}^T \nabla T_0$. Thus, the Cauchy-Green tensor and the initial tracer gradient completely determine the averaged squared norm of advected tracer gradients (equation (2.10)). To simplify the above expression, we define the angle between the tracer gradient and the compressive

(stable) direction of the direct flow as:

$$\cos(\theta_{T_0}^\phi) = \frac{(\mathbf{P}^T \nabla T_0)_2}{\|\nabla T_0\|_2}. \quad (2.12)$$

Finally, we infer the following compact expression:

$$\overline{\|\nabla T\|^2} - \overline{\|\nabla T_0\|^2} = \overline{\|\nabla T_0\|^2 \alpha^2 \left(1 + \frac{\beta}{\alpha} \cos(2\theta_{T_0}^\phi)\right)}. \quad (2.13)$$

The advection globally increases (decreases) the tracer gradient norm if the initial tracer gradient is locally close enough to the stable (unstable) direction of the direct flow. This corresponds to $\theta_{T_0}^\phi$ close to $0[\pi]$ or $\frac{\pi}{2}[\pi]$ respectively. This is modulated by the initial amplitude of the tracer gradients, α^2 and $\frac{\beta}{\alpha} = \sqrt{1 + \frac{2}{\alpha^2}} \geq 1$. It should be noticed that α and β do not explicitly depend on the tracer.

2.2 Decorrelation approximations

Over the space, the angle $\theta_{T_0}^\phi$ takes different values. If the flow gradients and the initial tracer gradients are not correlated and are oriented along various angles over the space, the variance of $\theta_{T_0}^\phi$ will likely be large (*i.e.* close to 2π). Then, due to the overlapping, the distribution of $2\theta_{T_0}^\phi[2\pi]$ over the space becomes close to an uniform law on $[0, 2\pi]$. The average over the space of the term $\cos(2\theta_{T_0}^\phi)$ will become close to zero, and

$$\overline{\|\nabla T\|^2} - \overline{\|\nabla T_0\|^2} \approx \overline{\|\nabla T_0\|^2 \alpha^2} > 0. \quad (2.14)$$

On average, the tracer gradients will thus always increase by stretching. Figure 1 illustrates well the process. The tracer is completely passive. It can be a dye or an oil spill introduced at time $t = 0$. In this case, the tracer and the flow are completely decorrelated and the initial structure of the tracer is quickly stretched and folded to fill a broad range of scales. In contrast, geophysical tracers are generally correlated to the flow. This correlation ensues from the previous advection (from time $t = -\infty$ until $t = 0$) which had led to the initial tracer T_0 and from the non-linear effects. It is expressed by the angle $\theta_{T_0}^\phi$ in the right-hand-side integrand of equation (2.13) which can be locally positive or negative. Accordingly, that correlation restricts or reduces locally enhanced strong gradients. In the Lagrangian advection method (Berti and Lapeyre, 2014; Dencausse et al., 2014), the tracers – Sea Surface Temperature (SST) or Sea Surface Salinity (SSS) – are not passive. The flow and the tracers are correlated. This is the reason of the preservation of the tracers' very-large-scale structures such as the background meridional gradient. However, at mesoscales and submesoscales, the initial tracer and the flow have been decorrelated by the filtering. So, our result (2.14) predicts a strengthening of mesoscale and submesoscale tracer gradients. This is exactly what is happening in the works of Berti and Lapeyre (2014) and Dencausse et al. (2014).

By assuming again no correlation between the initial tracer and the flow, the formula (2.14) can be further

approximated by:

$$\frac{\|\nabla T\|^2}{\|\nabla T_0\|^2} \approx 1 + \overline{\alpha^2}. \quad (2.15)$$

Before modeling the time dependance of the averaged growth rate, $\overline{\alpha^2}$, we describe the links between the mixing diagnostic introduced by Mezić et al. (2010) and our exact result (2.13).

2.3 Link with the mixing criterion of Mezić et al. (2010)

As in Mezić et al. (2010), the mesochronic velocity is defined as the velocity time-averaged along a trajectory:

$$\check{\mathbf{v}}(\mathbf{x}_0, t) \triangleq \frac{1}{t} \int_0^t dt' \mathbf{V}(\mathbf{x}_0, t') = \frac{\phi(\mathbf{x}_0) - \mathbf{x}_0}{t}, \quad (2.16)$$

where \mathbf{V} is the Lagrangian velocity. As derived by the authors, the incompressibility of the flow yields:

$$1 = \det(\nabla \phi^T) = \det(\mathbb{I}_d + t \nabla \check{\mathbf{v}}^T) = 1 + t \operatorname{tr}(\nabla \check{\mathbf{v}}^T) + t^2 \det(\nabla \check{\mathbf{v}}^T). \quad (2.17)$$

The mesochronic velocity is thus an incompressible flow with the following structure:

$$t \det(\nabla \check{\mathbf{v}}^T) = -\operatorname{tr}(\nabla \check{\mathbf{v}}^T) = -\nabla \cdot \check{\mathbf{v}} \neq 0. \quad (2.18)$$

The definition of the local growth rate, α^2 thus reads:

$$\alpha^2 \triangleq \frac{1}{2} \|\nabla \phi^T\|^2 - 1, \quad (2.19)$$

$$= \frac{1}{2} \|\mathbb{I}_d + t \nabla \check{\mathbf{v}}^T\|^2 - 1, \quad (2.20)$$

$$= -t(t \det(\nabla \check{\mathbf{v}}^T)) + \frac{t^2}{2} \|\nabla \check{\mathbf{v}}^T\|^2, \quad (2.21)$$

$$= \frac{t^2}{2} ((\partial_x \check{u} - \partial_y \check{v})^2 + (\partial_y \check{u} + \partial_x \check{v})^2). \quad (2.22)$$

It expresses the strain of the mesochronic velocity. Then, let us introduce the mesochronic vorticity $\check{\omega} \triangleq \nabla^\perp \cdot \check{\mathbf{v}}$. Note that the mesochronic vorticity is not the vorticity time-averaged along a trajectory. With this notation, the incompressibility constraint (2.18) enables us to rewrite equation (2.22) as a function of the determinant $\det(\nabla \check{\mathbf{v}}^T)$:

$$\alpha^2 = \frac{t^2}{2} ((\nabla \cdot \check{\mathbf{v}})^2 - 4 \det(\nabla \check{\mathbf{v}}^T) + \check{\omega}^2), \quad (2.23)$$

$$= \frac{t^2}{2} \left(t^2 \det(\nabla \check{\mathbf{v}}^T) \left(\det(\nabla \check{\mathbf{v}}^T) - \frac{4}{t^2} \right) + \check{\omega}^2 \right). \quad (2.24)$$

Mezić et al. (2010) then call mesoelliptic areas, areas over which the tracer gradients turn while keeping their norm unchanged, and mesohyperbolic areas, areas overwhich the gradients increase or decrease. According to (2.13), mesoelliptic regions are thus associated with zero growth rate α^2 , and expression (2.24) leads to the equality

$$\det(\nabla \check{\mathbf{v}}^T) \left(\det(\nabla \check{\mathbf{v}}^T) - \frac{4}{t^2} \right) = - \left(\frac{\check{\omega}}{t} \right)^2 \leq 0. \quad (2.25)$$

We thus retrieve, following a different approach, the criterion introduced by Mezić et al. (2010). Indeed, the authors separate mesohyperbolic areas from mesoelliptic areas depending on the sign of the following criterion:

$$\det(\nabla \check{\mathbf{v}}^T) \left(\det(\nabla \check{\mathbf{v}}^T) - \frac{4}{t^2} \right). \quad (2.26)$$

Here, our developments provide further understandings. For the mesoellipticity case, equation (2.25) relates the criterion (2.26) to the mesochronic vorticity $\check{\omega}$. Conversely, making use of (2.24) and (2.22), the separation between mesoelliptic and mesohyperbolic behaviors is given by the sign of:

$$t^2 \det(\nabla \check{\mathbf{v}}^T) \left(\det(\nabla \check{\mathbf{v}}^T) - \frac{4}{t^2} \right) = 2 \left(\frac{\alpha}{t} \right)^2 - \check{\omega}^2, \quad (2.27)$$

$$= (\partial_x \check{u} - \partial_y \check{v})^2 + (\partial_y \check{u} + \partial_x \check{v})^2 - \check{\omega}^2. \quad (2.28)$$

This interpretation then becomes reminiscent to the Okubo-Weiss criterion (Okubo, 1970; Weiss, 1991; Shivamoggi and van Heijst, 2011). Indeed, this separation explicits the competition between the strain and the rotation of the mesochronic velocity, encoded by α and $\check{\omega}$, respectively.

The mesohyperbolicity corresponds to a stretching. It occurs when two points become closer or diverge. This property is naturally encoded in:

$$\|\phi^{-1}(\mathbf{x} + \delta\mathbf{x}) - \phi^{-1}(\mathbf{x})\|^2 \approx \|[\nabla(\phi^{-1})^T(\mathbf{x})]\delta\mathbf{x}\|^2 = \delta\mathbf{x}^T ([\nabla\phi^T(\mathbf{y})][\nabla\phi^T(\mathbf{y})]^T)^{-1} \delta\mathbf{x}, \quad (2.29)$$

where $\mathbf{y} = \phi^{-1}(\mathbf{x})$. Mixing can occur when folding is associated with stretching. Folding is then obviously associated with a three-points kinematic property. First, the three points are separated by stretching, creating a filament. Then, the filaments folds bringing the two opposite points closer again. This folding can trap an area having a distinct tracer value creating strong tracer gradients. To identify mixing zones, Mezić et al. (2010) thus separate two types of mesohyperbolicity: the couples of points which have turned ($\delta\mathbf{x}^T (\phi(\mathbf{x} + \delta\mathbf{x}) - \phi(\mathbf{x})) < 0$) and the others ($\delta\mathbf{x}^T (\phi(\mathbf{x} + \delta\mathbf{x}) - \phi(\mathbf{x})) > 0$). An area where both types of mesohyperbolicity are present and adjacent must have been folded and hence corresponds to a mixing zone. To separate these two types of mesohyperbolicity, the authors study the eigenvalues of the evolution matrix $(\nabla\phi^T)^T$ instead of its singular values. Note however that folding could also be studied directly relying on the Cauchy-Green tensor, $[\nabla\phi^T][\nabla\phi^T]^T$. Indeed,

$$(\phi^{-1}(\mathbf{x} + \delta\mathbf{x}_1) - \phi^{-1}(\mathbf{x}))^T (\phi^{-1}(\mathbf{x} + \delta\mathbf{x}_2) - \phi^{-1}(\mathbf{x})) \approx \delta\mathbf{x}_1^T ([\nabla\phi^T(\mathbf{y})][\nabla\phi^T(\mathbf{y})]^T)^{-1} \delta\mathbf{x}_2, \quad (2.30)$$

where $\mathbf{y} = \phi^{-1}(\mathbf{x})$. Adequately normalized, this scalar product defines an angle between a pair of points. If the angle is smaller than the initial angle, defined by $\delta\mathbf{x}_1^T \delta\mathbf{x}_2$, folding occurs. Such criterion can be analytically expressed with eigenvectors and eigenvalues of the Cauchy-Green tensor.

To note, few other methods exist in the literature to diagnose folding and its relation to stretching. For instance, Budišić and Thiffeault (2015) study wrapping of advected points with braids. This mathematical tool provides simple visualizations of the number of winding of given sets of advected points relatively to other sets of points. As introduced, the Finite Time Braids Exponents (FTBE) then quantify the increasing rate of the number of windings. Following an other approach, Ma et al. (2016) directly measure folding of material lines through an analysis of their curvature variations. In the following, we relate folding, stretching and gradient of the curvature of streamlines in the case of a slowly varying Eulerian velocity field.

2.4 Time dependance

In the work of Dencausse et al. (2014), the time resolution of Eulerian velocity is relatively low. This is a common feature of velocity estimates from space. Today, their typical temporal resolution is about 10 days. Moreover, being associated with geostrophic dynamics, the velocity correlation time is generally about 1 month. Therefore, the velocity field does not vary much during an advection of one or two weeks. Hence, the velocity will be assumed stationary. This assumption determines a specific form for the flow. In particular, the flow is not chaotic (Thiffeault, 2004). The analysis will first separate between two typical cases: open straight streamlines and closed curved streamlines.

2.4.1 Locally uniform shear

Let us first focus on locally straight streamlines (*i.e.* streamlines with zero curvature). In such a case, the strengthening of tracer gradients results from a velocity shear, similarly to usual infinitesimal-time stretching. We denote by x the local axis of the straight streamline and by $v_x = \frac{\mathbf{v}}{\|\mathbf{v}\|} \cdot \mathbf{v} = \|\mathbf{v}\|$, the velocity component on this direction. The incompressibility imposes

$$\left(\frac{\mathbf{v}}{\|\mathbf{v}\|} \cdot \nabla \right) v_x = \partial_x v_x = \nabla \cdot \mathbf{v} = 0. \quad (2.31)$$

Thus, since the Eulerian velocity is stationary, the Lagrangian velocity is stationary as well:

$$\frac{d\mathbf{V}}{dt}(\mathbf{x}_0, t) = \frac{d}{dt} (\mathbf{v}(\phi(\mathbf{x}_0, t))) = ((\mathbf{v} \cdot \nabla) \mathbf{v})(\phi(\mathbf{x}_0, t)) = 0, \quad (2.32)$$

and the flow simplifies to

$$\phi(\mathbf{x}_0, t) = \mathbf{x}_0 + \int_0^t dt' V(\mathbf{x}_0, t') = \mathbf{x}_0 + v(\mathbf{x}_0)t. \quad (2.33)$$

This so-called ballistic regime is superdiffusive (Vallis, 2006; Falkovich et al., 2001). Taking the gradient of the above expression and, using the incompressibility again, the stretching rate reads

$$\alpha^2 \triangleq \frac{1}{2} \|\nabla \phi^T\|^2 - 1 = \frac{1}{2} \|\mathbb{I}_d + \nabla \mathbf{v}^T t\|^2 - 1 = \frac{t^2}{2} \|\nabla \mathbf{v}^T\|^2 = t^2 \underbrace{\frac{1}{2} \left(\frac{\mathbf{v}^\perp}{\|\mathbf{v}^\perp\|} \cdot \nabla \|\mathbf{v}\| \right)^2}_{=1/\tau_s^2}, \quad (2.34)$$

where the last equality comes from the orientation of velocity gradients imposed by (2.31). The time τ_s will be referred to as the shearing time.

2.4.2 Stationary convective cells

Close to vortices, streamlines are often closed or at least curved, and the previous development cannot be applied. For this purpose, we now focus on closed streamlines. Since the flow is incompressible, fluid parcels cannot accumulate. Therefore, those streamlines define loops, called stationary convective cells (Falkovich et al., 2001), where fluid parcels rotate periodically. Accordingly, the flow and thus the Lagrangian velocity are periodic and the flow is called subdiffusive (Vallis, 2006; Falkovich et al., 2001). This geometry can nevertheless create strong stretching in finite-time. Indeed, two concentric closed streamlines can define Lagrangian loops associated with different rotation periods. Rotations after rotations, a fluid parcel on the fastest loop will deviate from its initial neighboring parcel on the slowest loop. So, this differential rotation creates stretching. Moreover, it also induces folding. A filament distributed perpendicular to streamlines will be deformed by the continuous differential rotation. After a finite time, the filament will wrap around the convective cell creating spirals. Lehahn et al. (2007) illustrate a similar process with the action of stable and unstable manifolds on phytoplankton patches. To mathematically express the stretching induced by those convective cells, we propose to write the flow as follows:

$$\phi(\mathbf{x}_0) = \phi(\mathbf{x}_0, t) \approx \mathbf{x}_0 + \mathbf{g}(\mathbf{x}_0, f(\mathbf{x}_0)t), \quad (2.35)$$

where \mathbf{g} is 1-periodic with respect to its second variable and $f(\mathbf{x}_0)$ is the local temporal frequency. Accordingly, for a point initially on \mathbf{x}_0 in a closed streamline \mathcal{C} , the trajectory $t \mapsto \phi(\mathbf{x}_0, t)$ runs from \mathbf{x}_0 to \mathbf{x}_0 through a path \mathcal{P} embedded in \mathcal{C} with a temporal period $1/f(\mathbf{x}_0)$ defined by:

$$\frac{1}{f(\mathbf{x}_0)} = \int_0^{1/f(\mathbf{x}_0)} dt = \int_{\mathcal{P}} \frac{dl}{\|\mathbf{v}\|} = \oint_{\mathcal{C}} \frac{\mathbf{v}}{\|\mathbf{v}\|^2} \cdot d\mathbf{l} = \iint_{\mathcal{A}} \nabla^\perp \cdot \left(\frac{\mathbf{v}}{\|\mathbf{v}\|^2} \right) d\mathbf{A}, \quad (2.36)$$

where $\nabla^\perp \cdot$ denotes the two dimensional-curl and \mathcal{A} the surface delimited by \mathcal{C} . As the two last integrals only depend on the streamline \mathcal{C} and not on the precise initial condition \mathbf{x}_0 , the local frequency inherits from the same invariance. Since the Eulerian velocity is stationary, the points \mathbf{x}_0 and $\phi(\mathbf{x}_0, t)$ are on the same streamline, and thus:

$$f(\phi(\mathbf{x}_0, t)) = f(\mathbf{x}_0). \quad (2.37)$$

This frequency can be approximated by a local angular velocity $\dot{\theta}$, estimated using the streamline curvature, denoted $1/R$, as:

$$f \approx \frac{\dot{\theta}}{2\pi} \approx \frac{\|\mathbf{v}\|}{2\pi R} = \frac{1}{2\pi} \left[(\mathbf{v} \cdot \nabla) \frac{\mathbf{v}}{\|\mathbf{v}\|} \right] \cdot \frac{\mathbf{v}^\perp}{\|\mathbf{v}^\perp\|}. \quad (2.38)$$

In practice, since the exact formula (2.36) can be difficult to evaluate numerically, we will instead use the above approximation. In the following derivation, we however keep the exact definition (2.36). In particular, we still assume the frequency invariance along the streamline (2.37). The first coordinate of \mathbf{g} encodes the spatial dependency of the loop (vectorial) amplitudes. Note that the model (2.35) is very general as it only assumes periodicity of Lagrangian trajectories. It enables us to partially decouple flow variations associated with different streamlines (*i.e.* different local frequencies f) and flow variations associated with different temporal phase shift along the streamline (*i.e.* different times t). To some extent, this second type of variation can be understood as different initial conditions in the same streamline, due to the periodicity assumption. Similar decomposition ideas were proposed by Thiffeault (2004) for chaotic (non-periodic) flows. Denotes:

$$(\partial_1 \mathbf{g}^T)(\mathbf{z}_1, z_2) = \nabla_{\mathbf{z}_1} (\mathbf{g}^T(\mathbf{z}_1, z_2)) \text{ and } (\partial_2 \mathbf{g})(\mathbf{z}_1, z_2) = \partial_{z_2} (\mathbf{g}(\mathbf{z}_1, z_2)). \quad (2.39)$$

Note that both terms are 1-periodic with respect to its second variable. By the frequency invariance (2.37), we can replace $f(\mathbf{x}_0)$ by $f(\phi(\mathbf{x}_0, t))$ in the model (2.35):

$$\phi(\mathbf{x}_0, t) = \mathbf{x}_0 + \mathbf{g}(\mathbf{x}_0, f(\phi(\mathbf{x}_0, t))t). \quad (2.40)$$

Then, replacing back $f(\phi(\mathbf{x}_0, t))$ by $f(\mathbf{x}_0)$ after evaluating the gradient, the stretching of the flow reads:

$$\begin{aligned} \nabla \phi^T(\mathbf{x}_0, t) &= \mathbb{I}_d + (\partial_1 \mathbf{g}^T)(\mathbf{x}_0, f(\phi(\mathbf{x}_0, t))t) \\ &\quad + t \nabla \phi^T(\mathbf{x}_0, t) \nabla f(\phi(\mathbf{x}_0, t)) (\partial_2 \mathbf{g}^T)(\mathbf{x}_0, f(\phi(\mathbf{x}_0, t))t), \end{aligned} \quad (2.41)$$

$$\begin{aligned} &= \mathbb{I}_d + (\partial_1 \mathbf{g}^T)(\mathbf{x}_0, f(\mathbf{x}_0)t) \\ &\quad + t \nabla \phi^T(\mathbf{x}_0, t) \nabla f(\phi(\mathbf{x}_0, t)) (\partial_2 \mathbf{g}^T)(\mathbf{x}_0, f(\mathbf{x}_0)t). \end{aligned} \quad (2.42)$$

In the last equality, the second right-hand term is time-periodic and thus bounded. If we neglect its time variation, it writes

$$(\partial_1 \mathbf{g}^T)(\mathbf{x}_0, f(\mathbf{x}_0)t) \approx (\partial_1 \mathbf{g}^T)(\mathbf{x}_0, 0) = \nabla \phi^T(\mathbf{x}_0, 0) - \mathbb{I}_d = 0. \quad (2.43)$$

Introducing the original periodic model (2.35) into its definition, the Lagrangian velocity \mathbf{V} reads:

$$\mathbf{V}(\mathbf{x}_0, t) = \frac{d\phi(\mathbf{x}_0, t)}{dt} = f(\mathbf{x}_0)(\partial_2 \mathbf{g})(\mathbf{x}_0, f(\mathbf{x}_0)t). \quad (2.44)$$

Finally, the flow gradient expression (2.42) can be rewritten using equations (2.43) and (2.44):

$$\nabla \phi^T(\mathbf{x}_0, t) = \mathbb{I}_d + t \nabla \phi^T(\mathbf{x}_0, t) \frac{\nabla f(\phi(\mathbf{x}_0, t))}{f(\mathbf{x}_0)} \mathbf{V}^T(\mathbf{x}_0, t), \quad (2.45)$$

$$= \mathbb{I}_d + t \nabla \phi^T(\mathbf{x}_0, t) \left(\frac{1}{f} \nabla f \mathbf{v}^T \right) (\phi(\mathbf{x}_0, t)), \quad (2.46)$$

where the frequency invariance (2.37) was used in the last equality. After this, we factorize terms in $\nabla \phi^T$,

$$\mathbb{I}_d = \nabla \phi^T(\mathbf{x}_0, t) \left(\mathbb{I}_d - t \left(\frac{1}{f} \nabla f \mathbf{v}^T \right) (\phi(\mathbf{x}_0, t)) \right). \quad (2.47)$$

Then, we inverse the matrix equation and remap with the inverse flow, ϕ^{-1} :

$$(\nabla \phi^T)^{-1}(\phi^{-1}(\mathbf{x}, t), t) = \mathbb{I}_d - t \left(\frac{1}{f} \nabla f \mathbf{v}^T \right) (\mathbf{x}). \quad (2.48)$$

Note that since the frequency is a function of the streamline (2.37),

$$0 = \frac{d}{dt} (f(\mathbf{x}_0)) = \frac{d}{dt} (f(\phi(\mathbf{x}_0, t))) = (\mathbf{v} \cdot \nabla f)(\phi(\mathbf{x}_0, t), t). \quad (2.49)$$

Therefore, the frequency gradient is orthogonal to the velocity, and

$$\|\nabla f\| \approx \left| \frac{\mathbf{v}^\perp}{\|\mathbf{v}^\perp\|} \cdot \nabla f \right|. \quad (2.50)$$

As the eigenvalues of the flow gradients $\nabla \phi^T$ are the inverse of one another, this matrix and its inverse have the same Frobenius norm. So, the time dependance of the growth rate in the final grid (points \mathbf{x}) follows from its definition and from (2.48):

$$\alpha^2(\phi^{-1}(\mathbf{x}, t), t) \triangleq \frac{1}{2} \|\nabla \phi^T(\phi^{-1}(\mathbf{x}, t), t)\|^2 - 1, \quad (2.51)$$

$$= \frac{1}{2} \|(\nabla \phi^T)^{-1}(\phi^{-1}(\mathbf{x}, t), t)\|^2 - 1, \quad (2.52)$$

$$= - \underbrace{\left(\frac{t}{f} \nabla f \cdot \mathbf{v} \right) (\mathbf{x})}_{=0 \text{ by (2.49)}} + \underbrace{\left(\frac{t^2}{2f^2} \|\nabla f\|^2 \|\mathbf{v}\|^2 \right) (\mathbf{x})}_{=1/\tau_f^2}, \quad (2.53)$$

where τ_f will be referred to as the folding time. As (2.15) only involves the spatial average of α^2 , we can further simplify the model by spatial integration. By integrating equation (2.53) over a specific domain Ω_f , we can conclude with the variable change defined by the incompressible flow:

$$\int_{\Omega_f} d\mathbf{x}_0 \alpha^2(\mathbf{x}_0, t) = \int_{\phi(\Omega_f)} d\mathbf{x}_0 \alpha^2(\phi^{-1}(\mathbf{x}, t), t) = t^2 \int_{\phi(\Omega_f)} \frac{d\mathbf{x}}{\tau_f^2(\mathbf{x})}. \quad (2.54)$$

The subspace Ω_f is a subset of Ω where the concept of wrapping convective cells is relevant. Since we considered closed streamlines, we assume that $\phi(\Omega_f) = \Omega_f$. This subspace will be properly defined in the

following.

2.4.3 Global time dependence

In order to combine the folding time, τ_f , and the shearing time, τ_s , we locally define a local stretching time τ :

$$\tau(\mathbf{x}_0) \triangleq \begin{cases} \tau_f(\mathbf{x}_0) & \text{if } R(\mathbf{x}_0) \leq \frac{L}{2} \\ \tau_s(\mathbf{x}_0) & \text{if } R(\mathbf{x}_0) > \frac{L}{2} \end{cases}, \quad (2.55)$$

where $1/R(\mathbf{x}_0)$ is the streamline curvature on \mathbf{x}_0 , L the average diameter of a vortex. Following the previous models of shearing and folding, we model the stretching rate by:

$$\alpha = \frac{t}{\tau}. \quad (2.56)$$

Where gradients are created by a uniform shear, streamlines are straight, the curvature $1/R$ is weak and $\tau = \tau_s$, whereas, where the gradients strengthen by wrapping, the curvature is larger and $\tau = \tau_f$. To estimate the average vortices diameter L , we make uses of a toy model:

$$\mathbf{v} = U \begin{pmatrix} \cos\left(\frac{2\pi}{\lambda}x\right) \sin\left(\frac{2\pi}{\lambda}y\right) \\ \sin\left(\frac{2\pi}{\lambda}x\right) \cos\left(\frac{2\pi}{\lambda}y\right) \end{pmatrix}. \quad (2.57)$$

The vortices diameter is identified to the size of the convective cell:

$$L = \frac{\lambda}{2} = \left(\frac{6\pi^2 \|\mathbf{v}\|^2}{\|\nabla \mathbf{v}^T\|^2} \right)^{1/2}. \quad (2.58)$$

We use this diameter estimator in the general case.

The condition (2.55) well defines a space partition $\Omega = \Omega_f \cup \Omega_s$ to integrate the growth rate α^2 :

$$\overline{\alpha^2} = \left(\frac{t}{\tau_G} \right)^2 \text{ with } \frac{1}{\tau_G^2} \triangleq \overline{\left(\frac{1}{\tau^2} \right)} = \frac{1}{S} \mathbb{E} \left(\int_{\Omega_f} \frac{d\mathbf{x}}{\tau_f^2(\mathbf{x})} + \int_{\Omega_s} \frac{d\mathbf{x}_0}{\tau_f^2(\mathbf{x}_0)} \right), \quad (2.59)$$

where $\Omega_f \triangleq \{\mathbf{x} \in \Omega | R(\mathbf{x}) \leq \frac{L}{2}\}$ and $\Omega_s \triangleq \{\mathbf{x}_0 \in \Omega | R(\mathbf{x}_0) > \frac{L}{2}\}$. Again, we assumed that $\phi(\Omega_f) = \Omega_f$ because the flow maps closed streamlines onto themselves. In the following, we will refer to τ_G as the global stretching time. The model (2.59) together with the folding and shearing time definitions (2.53)-(2.34) specify a global Eulerian estimate of finite-time stretching. Unlike usual diagnosis, such as FTLE and Finite Size Lyapunov Exponents (FSLE) (d'Ovidio et al., 2009), the proposed global model does not require any integration of the flow.

According to (2.15), the evolution law (2.59) determines the tracer gradient norm:

$$\frac{\overline{\|\nabla T\|^2}}{\|\nabla T_0\|^2} \approx 1 + \left(\frac{t}{\tau_G} \right)^2. \quad (2.60)$$

2.5 Numerical illustrations

Let us first exemplify these analytical developments with an instructive toy example, before dealing with satellite observations. We advected a large tracer filament by a stationary velocity field using a backward Lagrangian advection (Figure 2). For technical details on this method, we referred to Berti and Lapeyre (2014) and Dencausse et al. (2014). The tracer progressively wraps, eventually creating infinitely long filaments. With the formula (2.59), we estimate a global stretching time of 13.36 days. This roughly corresponds to half a rotation.

Figure 3 represents the spatial distribution of the stretching rate α^2 , the factor α/β and the mesochronic vorticity $\tilde{\omega}$ at several times for our toy model. The spatial distribution of α stabilizes after one week only. As demonstrated, this non-dimentionalized number is significant on the folding area (the border of the vortex). The ratio $\alpha/\beta = \sqrt{1 + \frac{2}{\alpha^2}}$ – which quantifies the significance of the orientation of tracer gradient – decreases along time in the mixing area. It stabilizes to its minimum value, say 1, at $t \approx \tau_G$. The mesochronic vorticity is first concentrated in the center of the cylinder. Then, after each global stretching time, a new ring of mesochronic vorticity is added to the mixing area.

Figure (4) displays the spatial distribution of the folding time, τ_f , the shearing time, τ_s , and the stretching time, τ , for this toy model. Folding and stretching time are represented both in the initial grid (\mathbf{x}_0) and in the advected grid ($\mathbf{x} = \phi(\mathbf{x}_0, t)$). This remapping on the initial grid is needed as the folding time is locally defined in the advected grid (see (2.53) and (2.54)). For this remapping, we integrated the forward flow $\mathbf{x}_0 \mapsto \phi(\mathbf{x}_0, t)$. Note that the remapping enables a better visualization of the stretching spatial distribution, but this mapping is not necessary for the global stretching time computation (2.59). The folding effects are dominant in this toy model and the folding time well captures the spatial structure of α^2 . Yet, the inverse folding time diverges outside of the vortex as the streamline curvatures tend to zero. Indeed, according to (2.38) zero curvature implies zero local frequency f and thus infinite folding time (see (2.53)). For such a weak curvature, the relevant model is the uniform shear. Following the space partition (2.55), the stretching time is chosen as a shearing time in these areas. The global models of time evolution of the averaged stretching rate (2.59) and of the tracer gradients (2.60) are also successfully tested in Figure 5.

We now perform a similar analysis using satellite data. Velocities are estimated from altimeter-derived SSH fields. The velocity field, on which the Eulerian estimates will be applied, corresponds to January 1st, 2011, in the Antarctic Circumpolar Current (ACC) region, south of Australia. We begin by a small spatial window of $10^\circ \times 10^\circ$. A larger window will be considered subsequently. Figure 6 delineates the Kinetic energy (KE) and the vorticity fields. The KE shows the ACC eastward jet between latitudes -50° and -48° . Two (warm) anticyclones and a (cold) depression are also visible both in the vorticity and in initial SST fields at $(129^\circ, -51^\circ)$, $(131^\circ, -54^\circ)$ and $(130.5^\circ, -49.5^\circ)$, respectively. We then advect the January 1st, 2011, SST field. Similarly to Dencausse et al. (2014), we linearly interpolate in time the daily velocity data to perform the advection operation. The vortice dipole closed to the jet creates a mushroom-like structure in the advected tracer. Each vortice wraps the tracer, creating spirals. The small southern anticyclone $(131^\circ, -54^\circ)$ seems weaker than the other anticyclone $(129^\circ, -51^\circ)$. Yet, it faster wraps the tracer, as velocities are certainly larger than over the dipole area.

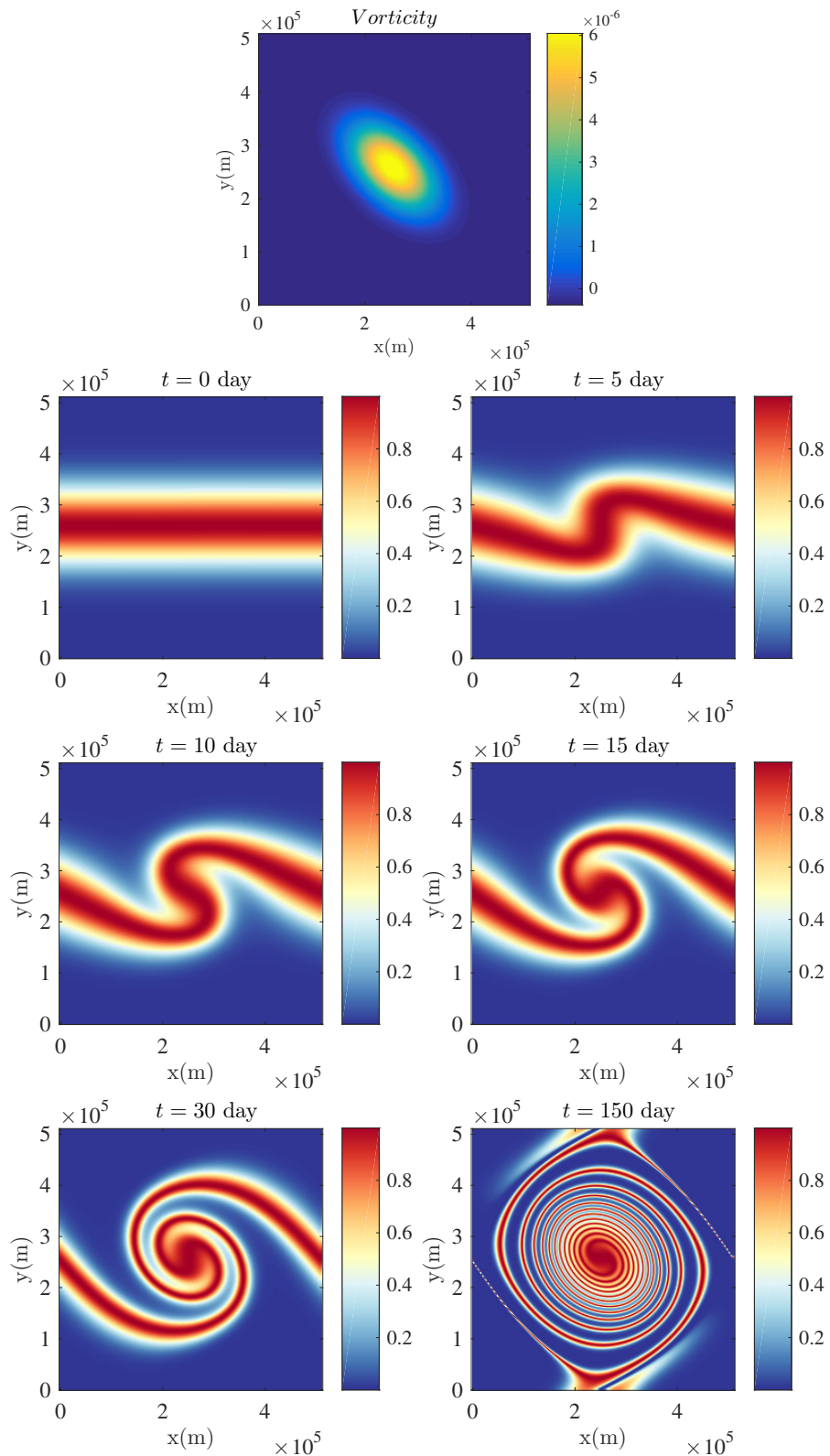


Figure 2: Advecting vorticity of the toy model (top in s^{-1}) and tracer (dimensionless) advected using a backward Lagrangian method at time $t = 0, 5, 10, 15, 30$ and 150 days.

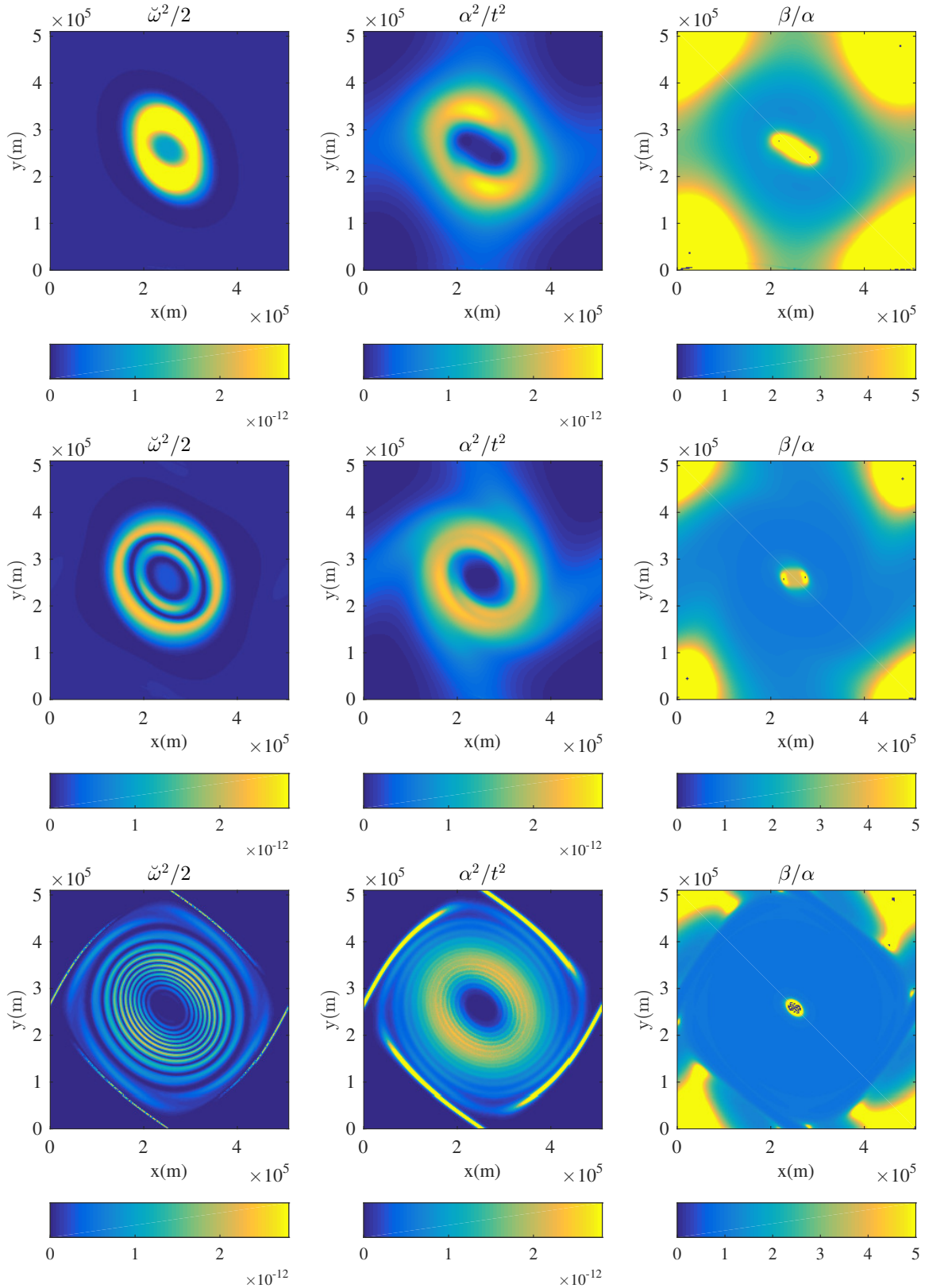


Figure 3: Values of $\tilde{\omega}^2/2$ (s^{-2}) (left), $(\alpha/t)^2$ (s^{-2}) (middle) and the ratio of α/β (dimensionless) (right) in the initial grid (points \mathbf{x}_0) at time (from top to bottom) $t = 15, 30$ and 150 days for the toy model.

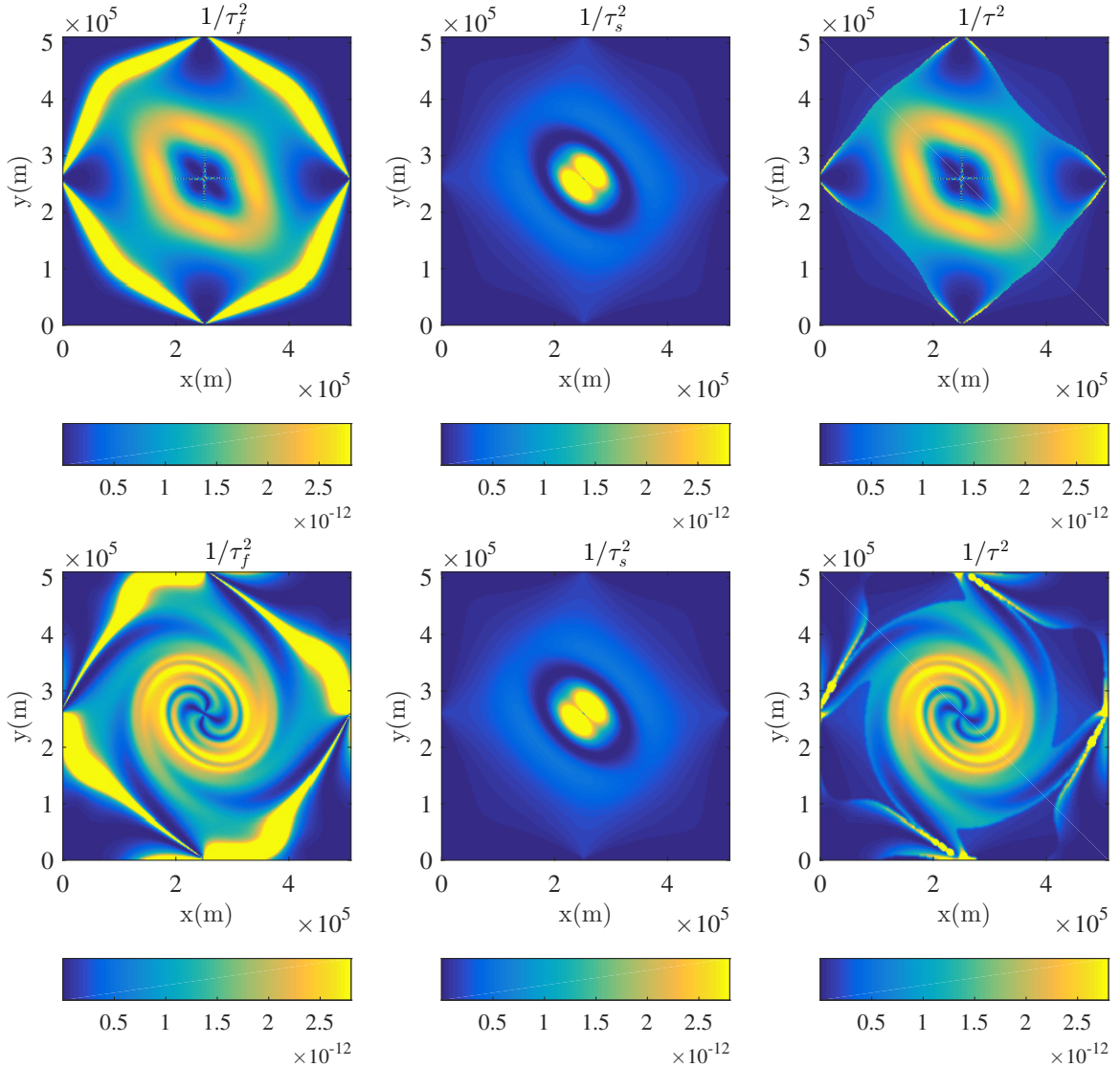


Figure 4: Squared inverse of the folding time in the final grid (points \mathbf{x}) (top left) and initial grid (points \mathbf{x}_0) (bottom left), the shearing in the initial grid (points \mathbf{x}_0) (top and bottom middle) and the stretching time in the final grid (points \mathbf{x}) (top right) and initial grid (points \mathbf{x}_0) (bottom right) for the toy model. All plots are in s^{-2} . In order to represent folding and stretching time in the initial grid, these fields were advected during 30 days.

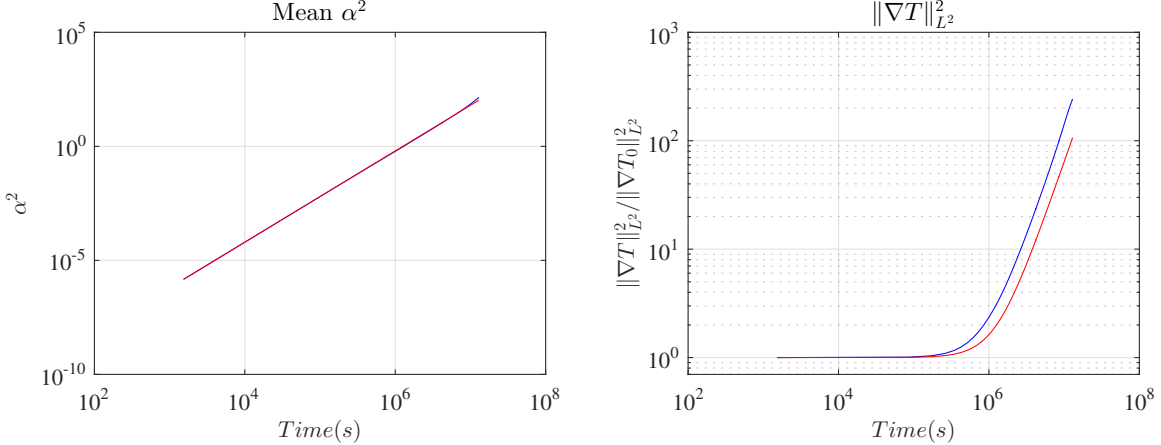


Figure 5: The averaged growth rate, $\overline{\alpha^2}$, (left) and the averaged squared norm of tracer gradients for the toy model, both in log-log plot along time. The blue line is the real value and the red line our model.

Figure 7 shows the stretching rate, α , the mesochronic vorticity, $\tilde{\omega}$, and the estimate (weighting) of the tracer/flow correlation, β/α . The folding, shearing and stretching time are presented in the same Figure. A slight low-pass spatial filtering (2-km filter width) is applied to the stretching time to help distinguish the filamentous structures. The spatial distributions of stretching rate and stretching time are very similar. The amplitude of the stretching time is slightly underestimated (ratio of about 2). The sides of the aforementioned vortices exhibit intense mixing, whereas the inverse shearing time is weak. As for the toy model, folding effects due to differential rotations near the boundaries of vortices are the leading mixing processes.

Now, we consider a larger space window to visualize a broader variety of structures and dynamical processes. The spatial location and the date remain the same. Figure 8 displays the KE and the vorticity. The jet and many vortices are visible. In the same manner, the SST is advected (Figure 9). The advection creates small-scale structures which turn to unphysical spirals when the advection time is too long. At 48 days of advection the advected domain is strongly deformed, especially by the eastward jet. Figure 10 compares the stretching ratio, α^2 , and the estimated stretching time in this larger spatial window. As found, most stretching structures are well predicted by the proposed model.

Finally, Figure 11 presents the time evolution of the averaged stretching rate (2.59) and of the averaged tracer gradients norm (2.60). The reference plots clearly exhibit the structures prescribed by models (11) and (2.59):

$$\overline{\alpha^2} = \left(\frac{t}{\tau_G} \right)^2 \text{ and } \frac{\|\nabla T\|^2}{\|\nabla T_0\|^2} = \begin{cases} 1 & \text{if } t \ll \tau_G \\ \left(\frac{t}{\tau_G} \right)^2 & \text{if } t \gg \tau_G \end{cases}. \quad (2.61)$$

We estimate a global stretching time of 1.67 days and the plots reveal a good match even though the stretching time seems slightly underestimated (by a factor of about ~ 1.7). The small shift between predicted and reference averaged tracer gradients norm may also be explained by a residual correlation between the tracer and the underlying flow as explained previously with equation (2.13).

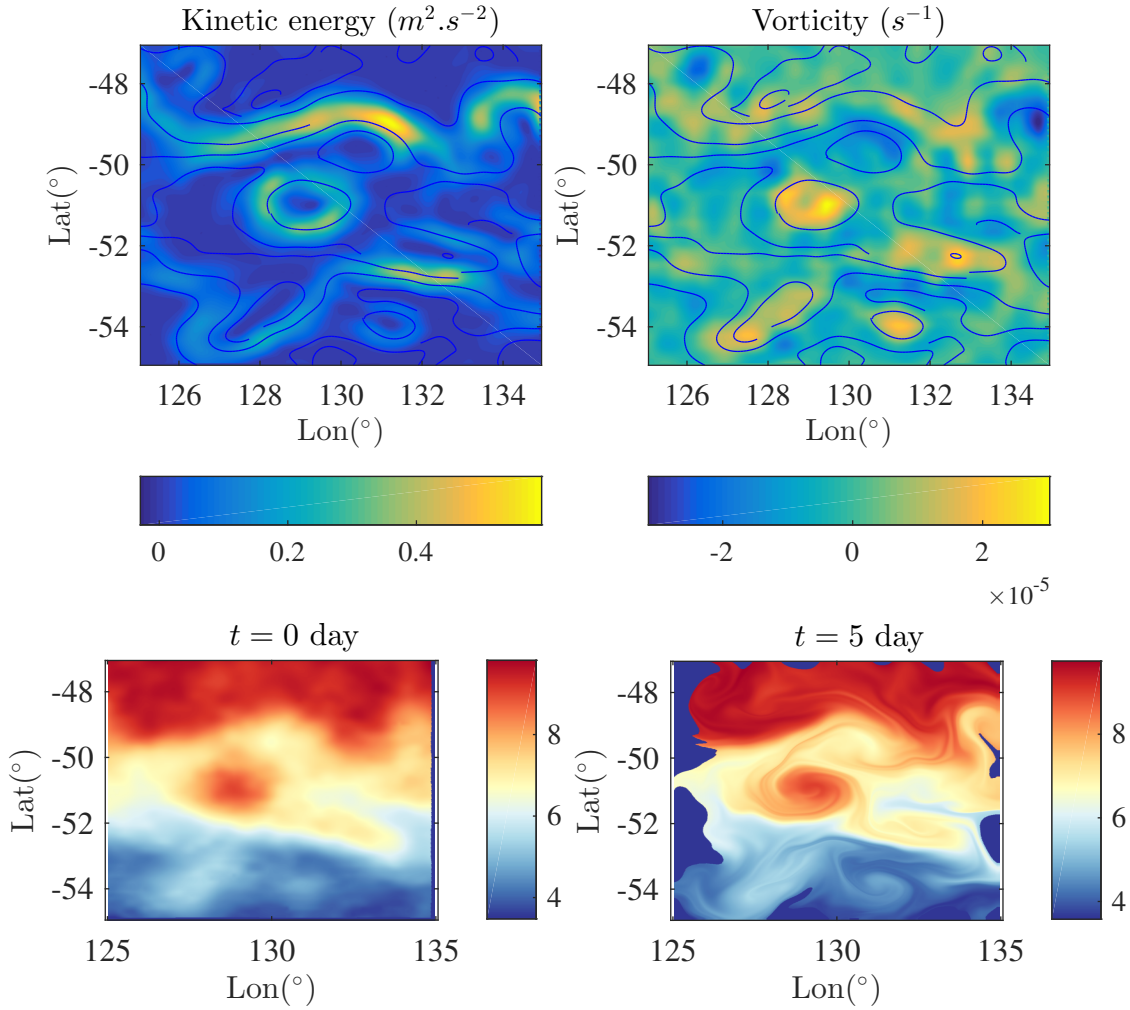


Figure 6: Kinetic energy (KE) (top left in $m^2.s^{-2}$), vorticity (top right in s^{-1}), SST (bottom left in $^{\circ}\text{C}$), all measured by satellite the 1st of January 2011, and SST (in $^{\circ}\text{C}$) after a 5-day advection (bottom right). On the top images, streamlines are superimposed. The streamlines, the KE, the vorticity and the advection are defined by SSH-derived velocity fields.

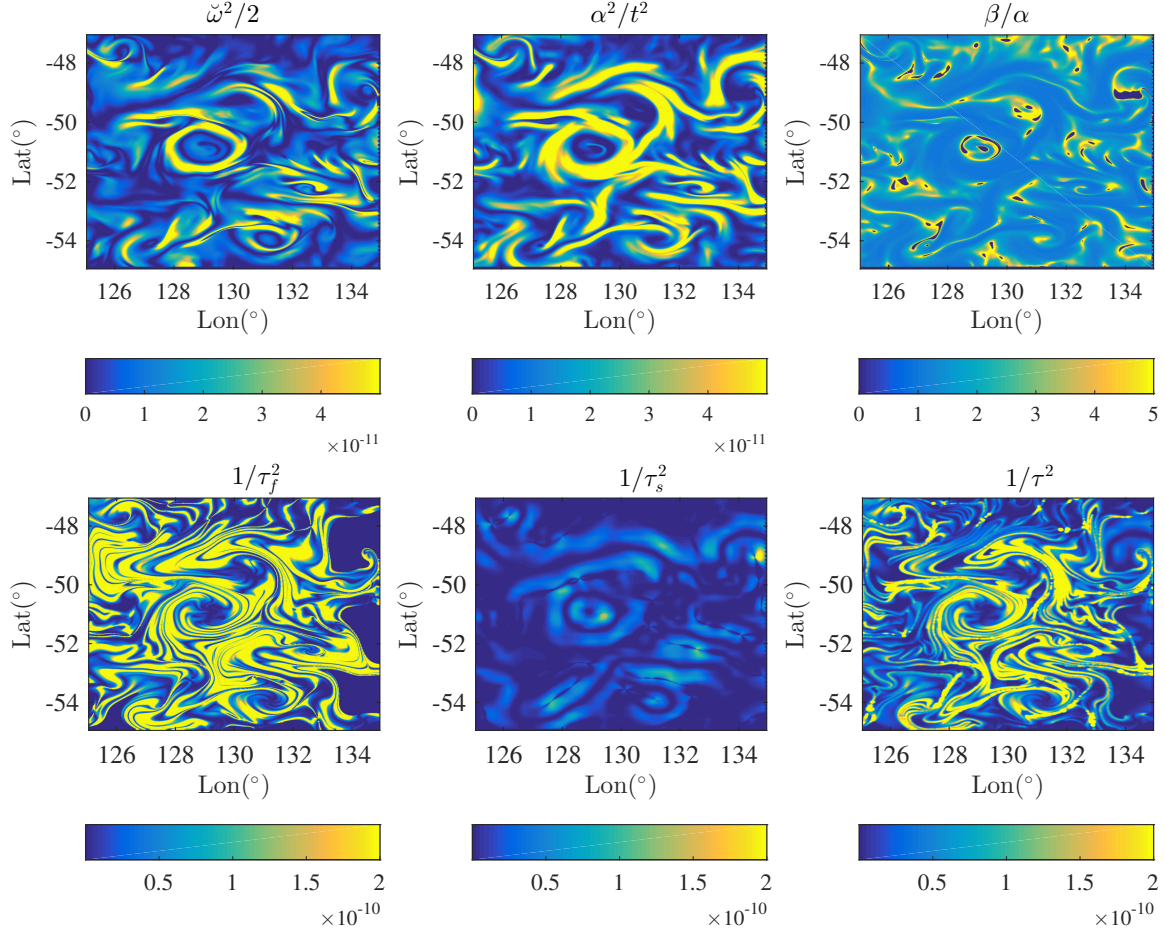


Figure 7: Values of the mesochronic vorticity, $\tilde{\omega}^2/2$, (s^{-2}) (top left), the stretching growth rate, $(\alpha/t)^2$, (s^{-2}) (top middle), the ratio α/β (dimensionless) (top right), the squared inverse of the folding time (s^{-2}) (bottom left), the shearing time (s^{-2}) (bottom middle) and the stretching time (s^{-2}) (bottom right), in the initial grid (points x_0) at time $t = 5$ days for the SSH-derived velocity fields. We can observe the good match between the stretching rate and our Eulerian estimation of the stretching time.

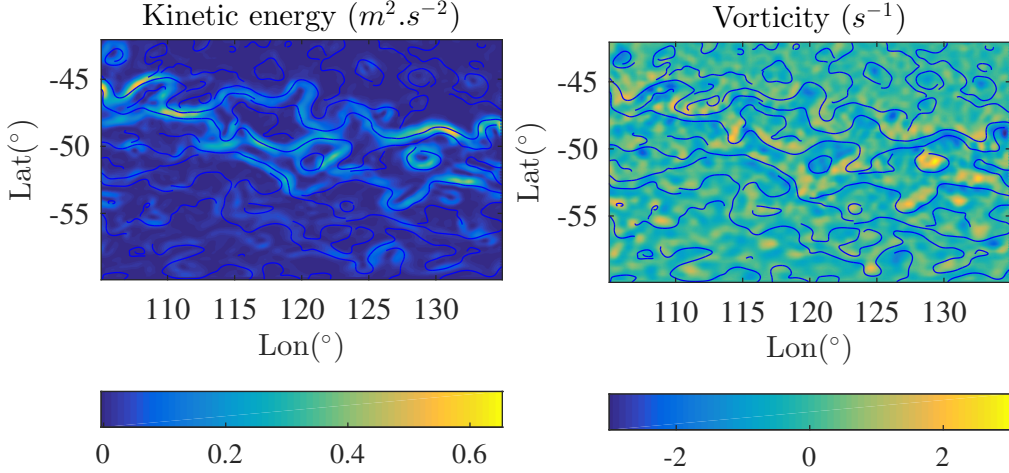


Figure 8: Kinetic energy (KE) (left in $m^2.s^{-2}$) and vorticity (right in s^{-1}) derived from SSH measured the 1st of January 2011.

3 Tracer spectral tail

In the following, we study the distortion of scales of the tracer T during the advection, *i.e.* the evolution of its spectral tail. The main results of this section does not necessitate to consider the decorrelation assumption of 2.2, nor the stationary assumption used in 2.4.2. Developments are thus more general. After preliminary results related to tracer moments, we first derive a Gaussian approximation for the evolution of the spectrum tail, assuming spatial smoothness. This approximation is then applied to initial and advected tracers. Finally, we generalize the development and discussion to self-similar spectra.

3.1 Moment conservation

In the following, \hat{T}_0 , \hat{T} , γ_{T_0} , γ_T and Γ_{T_0} , Γ_T denote the Fourier transforms, the covariances (associated with the averaging \bullet) and the spectra of initial and final tracer fields, respectively. Furthermore, the Hessian of a function f will be denoted by \mathbf{H}_f . It is interesting to remark that the tracer mean, \bar{T} , does not change during the advection. Indeed, for the advected tracer $T(\mathbf{x}) = T_0(\phi^{-1}(\mathbf{x}))$, the variable change defined by the inverse flow $\mathbf{x} \rightarrow \phi^{-1}(\mathbf{x}) = \mathbf{x}_0$ and the incompressibility constraint ($\det(\nabla\phi^T) = 1$) yields:

$$\bar{T} = \frac{1}{S} \mathbb{E} \int_{\Omega} d\mathbf{x} T(\mathbf{x}) = \frac{1}{S} \mathbb{E} \int_{\Omega} d\mathbf{x}_0 \underbrace{\frac{1}{\det(\nabla\phi^T(\mathbf{x}_0))}}_{=1} T_0(\mathbf{x}_0) = \bar{T}_0. \quad (3.1)$$

As a consequence, we will assume without loss of generality that the tracer is centered. Similarly, the (spatial) variance conservation can be deduced:

$$\gamma_T(0) = \bar{T}^2 = \frac{1}{S} \mathbb{E} \int_{\Omega} d\mathbf{x} T^2(\mathbf{x}) = \frac{1}{S} \mathbb{E} \int_{\Omega} d\mathbf{x}_0 T_0^2(\mathbf{x}_0) = \bar{T}_0^2. \quad (3.2)$$

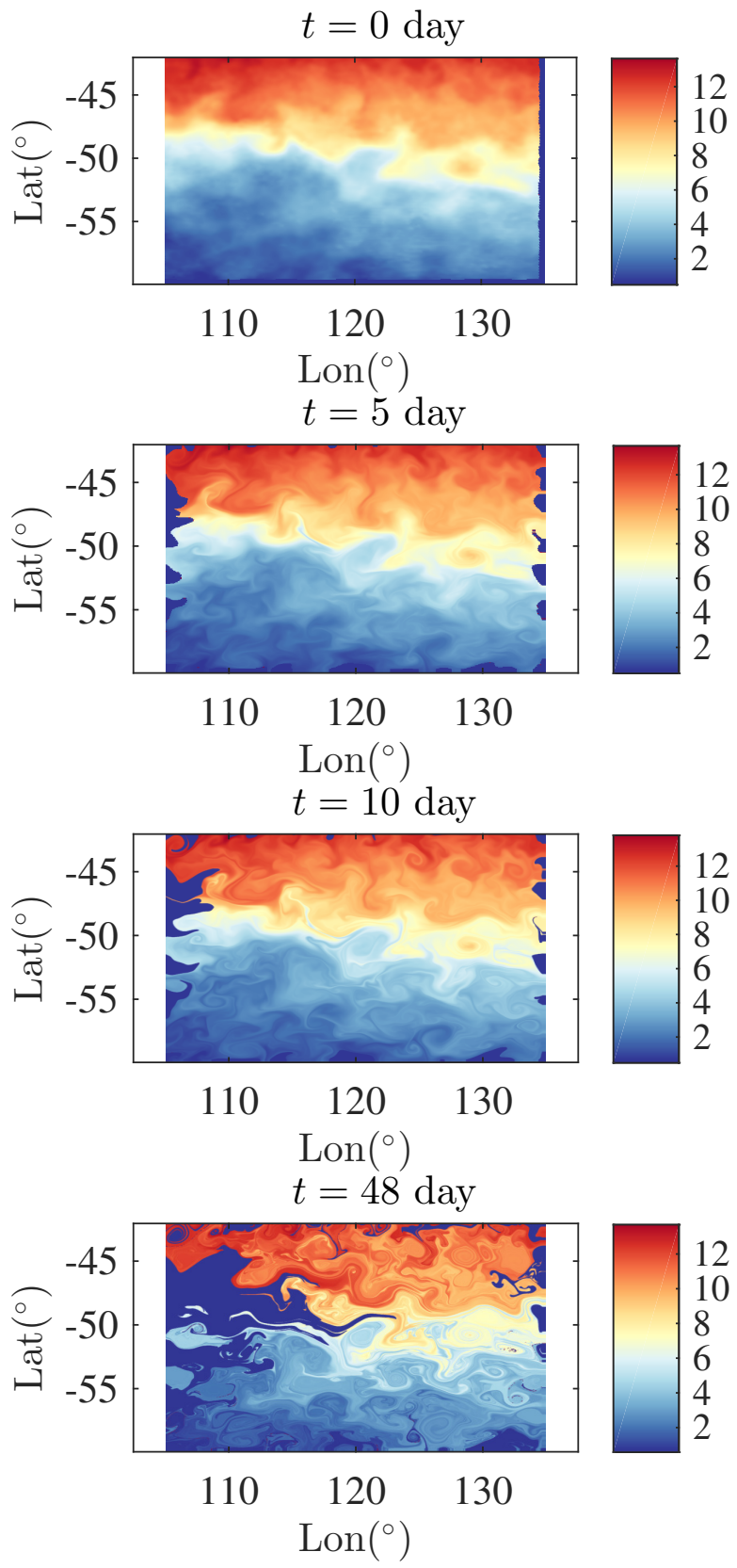


Figure 9: SST (in $^{\circ}\text{C}$) (from top to bottom) measured by satellite the 1st of January 2011, after 5-, 10-, and 48-day advection.

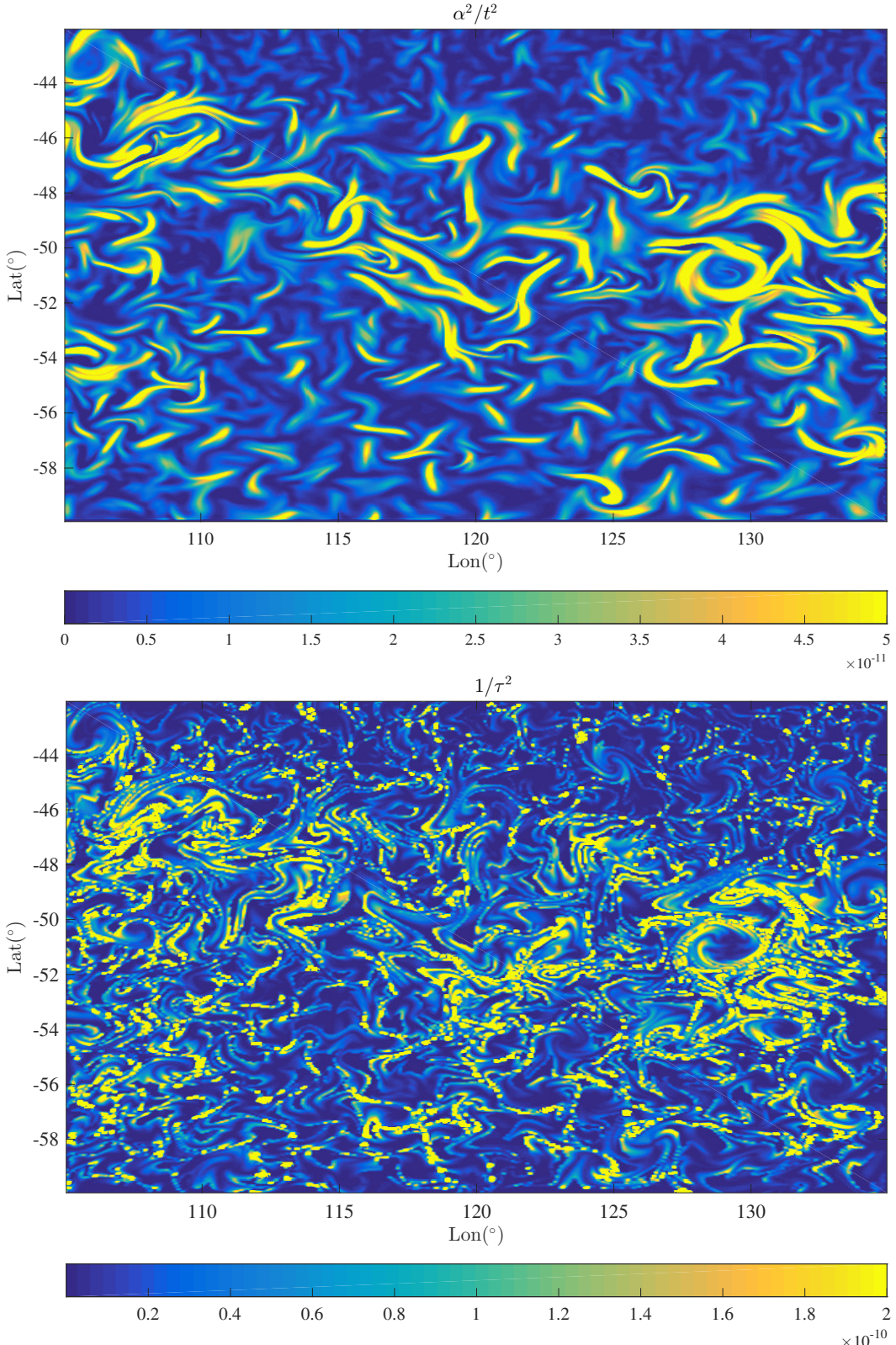


Figure 10: The stretching growth rate $(\alpha/t)^2$ (s^{-2}) (top) and the squared inverse of the stretching time, $1/\tau^2$, (s^{-2}) (bottom), in the initial grid (points \mathbf{x}_0) at time $t = 5$ days.

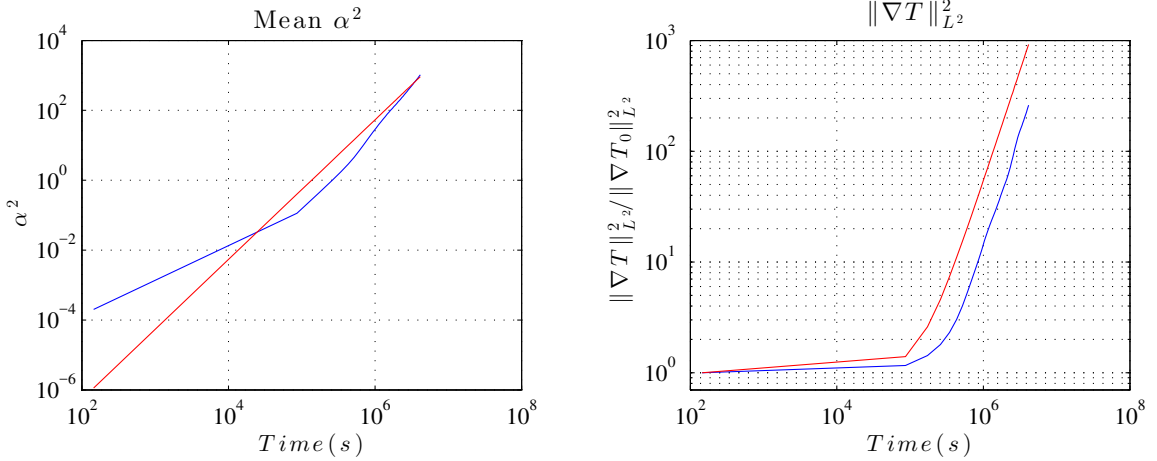


Figure 11: The averaged stretching rate, $\overline{\alpha^2}$, (left) and the ratio of squared-norm mean of tracer gradients, $\frac{\|\nabla T\|^2}{\|\nabla T_0\|^2}$ for the satellite data, both in log-log plot along time. The blue line is the real value and the red line our model.

Since all scales are assumed to be resolved and the molecular diffusion is ineffective on the length and time scales of interest, there are no overlays of fluid parcels and no dilution of their properties. Each fluid parcel conserves its tracer value during its advection. More generally, for all functions f , $\overline{f(T)}$ is conserved.

3.2 Smooth scalar approximation

First, let us consider the covariance of a smooth scalar f , for small spatial distance $\|\delta \mathbf{x}\|$. More specifically, we assume this covariance to be three times differentiable, which is a strong assumption on the scalar initial regularity. Yet, for tracers measured at mesoscales and re-interpolated on a submesoscale spatial grid, this assumption is still relevant. The covariance can then be approximated near 0 by its Taylor expansion:

$$\gamma_f(\delta \mathbf{x}) \triangleq \frac{1}{S} \mathbb{E} \int_{\Omega} d\mathbf{x} f(\mathbf{x}) f(\mathbf{x} + \delta \mathbf{x}), \quad (3.3)$$

$$= \overline{\|f\|^2} + \frac{1}{2} \delta \mathbf{x}^T \mathbf{H}_{\gamma_f}(0) \delta \mathbf{x} + \underset{\|\delta \mathbf{x}\| \rightarrow 0}{O}(\|\delta \mathbf{x}\|^3), \quad (3.4)$$

$$= \overline{\|f\|^2} \exp \left(-\frac{1}{2} \delta \mathbf{x}^T \left(\frac{-\mathbf{H}_{\gamma_f}(0)}{\|f\|^2} \right) \delta \mathbf{x} \right) + \underset{\|\delta \mathbf{x}\| \rightarrow 0}{O}(\|\delta \mathbf{x}\|^3), \quad (3.5)$$

where, by integration by parts:

$$-\mathbf{H}_{\gamma_f}(0) = -(\nabla_{\delta\mathbf{x}} \nabla_{\delta\mathbf{x}}^T \gamma_f(\delta\mathbf{x}))_{|\delta_x=0}, \quad (3.6)$$

$$= -\frac{1}{S} \mathbb{E} \int_{\Omega} d\mathbf{x} f(\mathbf{x}) (\nabla_{\delta\mathbf{x}} \nabla_{\delta\mathbf{x}}^T f(\mathbf{x} + \delta\mathbf{x}))_{|\delta_x=0}, \quad (3.7)$$

$$= -\frac{1}{S} \mathbb{E} \int_{\Omega} d\mathbf{x} f(\mathbf{x}) \mathbf{H}_f(\mathbf{x}), \quad (3.8)$$

$$= \frac{1}{S} \mathbb{E} \int_{\Omega} d\mathbf{x} \nabla f(\mathbf{x}) (\nabla f(\mathbf{x}))^T > 0 \text{ (in the Lowner sense).} \quad (3.9)$$

Hence, $-\overline{\|f\|^2} \mathbf{H}_{\gamma_f}^{-1}(0)$ encodes the square of the correlation lengths of the tracer, and the covariance can be approximated by a Gaussian function near 0. The Fourier transform of the covariance expression (3.5) provides the approximation if the spectrum tail, as:

$$\Gamma_f(\mathbf{k}) \triangleq \frac{1}{S} \mathbb{E} |\hat{T}_0(\mathbf{k})|^2, \quad (3.10)$$

$$= \frac{1}{S} \mathbb{E} \left| \int_{\Omega} d\mathbf{x} f(\mathbf{x}) e^{-i\mathbf{k}\cdot\mathbf{x}} \right|^2, \quad (3.11)$$

$$= \hat{\gamma}_f(\mathbf{k}), \quad (3.12)$$

$$\underset{\|\mathbf{k}\| \rightarrow \infty}{\sim} \frac{2\pi \left(\overline{\|f\|^2} \right)^2}{\det(\mathbf{H}_{\gamma_f}(0))^{\frac{1}{2}}} \exp \left(-\frac{1}{2} \mathbf{k}^T \left(-\overline{\|f\|^2} \mathbf{H}_{\gamma_f}^{-1}(0) \right) \mathbf{k} \right). \quad (3.13)$$

Note that the evolution of the opposite of the Hessian $-\mathbf{H}_{\gamma_f}(0) = \overline{\nabla f(\nabla f)^T}$ is much more difficult to describe than its trace. Indeed, equation (3.9) yields:

$$\text{tr}(-\mathbf{H}_{\gamma_f}(0)) = \overline{\text{tr}(\nabla f(\nabla f)^T)} = \overline{\|\nabla f\|^2}, \quad (3.14)$$

To let this gradient norm to appear, instead of the covariance Hessian, we consider the omnidirectional spectrum. The omnidirectional spectrum of the scalar f is defined as follows:

$$\bar{\Gamma}_f(\kappa) \triangleq \kappa \oint_{[0,2\pi]} d\theta_{\mathbf{k}} \Gamma_f(\mathbf{k}), \quad (3.15)$$

where $\mathbf{k} = \kappa \begin{pmatrix} \cos(\theta_{\mathbf{k}}) \\ \sin(\theta_{\mathbf{k}}) \end{pmatrix}$ is the wavenumber-vector and κ the wavenumber. As shown in the Appendix A, the Taylor expansion (3.5) then leads to:

$$\bar{\Gamma}_f(\kappa) \underset{\|\mathbf{k}\| \rightarrow \infty}{\sim} C_f \exp \left(-\frac{1}{2} L_f^2 \kappa^2 \right), \quad (3.16)$$

where

$$L_f^2 = \frac{\overline{\|f\|^2}}{\overline{\|\nabla f\|^2}} \text{ and } C_f = 2 \left(\frac{(2\pi)^3 \left(\overline{\|f\|^2} \right)^3}{\overline{\|\nabla f\|^2}} \right)^{1/2}. \quad (3.17)$$

3.3 Tail change

Applied, to both the initial tracer, T_0 , and the advected tracer, T , the approximation (3.16) yields:

$$\bar{\Gamma}_T(\kappa) \underset{\|\mathbf{k}\| \rightarrow \infty}{\sim} \bar{\Gamma}_{T_0}(\kappa) \frac{C_T}{C_{T_0}} \exp\left(-\frac{1}{2} (L_T^2 - L_{T_0}^2) \kappa^2\right), \quad (3.18)$$

$$\underset{\|\mathbf{k}\| \rightarrow \infty}{\sim} \bar{\Gamma}_{T_0}(\kappa) \left(\frac{\|\nabla T_0\|^2}{\|\nabla T\|^2} \right)^{1/2} \exp\left(\frac{1}{2} \frac{\|T_0\|^2}{\|\nabla T_0\|^2} \left(\frac{1}{\|\nabla T_0\|^2} - \frac{1}{\|\nabla T\|^2} \right) \kappa^2\right), \quad (3.19)$$

where the simplification in the last asymptotic equivalence is due to the variance conservation (3.2). As explained in section 2, if the initial tracer T_0 and the flow are decorrelated, the tracer gradients strengthen: $\|\nabla T\|^2 > \|\nabla T_0\|^2$ (*i.e.* $L_T < L_{T_0}$) and by (3.19) the tracer spectral tail raises. More precisely, using the estimate (2.60), we get for final expression:

$$\bar{\Gamma}_T(\kappa) \underset{\|\mathbf{k}\| \rightarrow \infty}{\sim} \bar{\Gamma}_{T_0}(\kappa) \left(1 + \left(\frac{t}{\tau_G}\right)^2\right)^{-1/2} \exp\left(\frac{1}{2} \frac{\|T_0\|^2}{\|\nabla T_0\|^2} \frac{\kappa^2}{1 + (\frac{\tau_G}{t})^2}\right). \quad (3.20)$$

This is illustrated for the toy flow in Figure (3.20). The Gaussian approximation successfully captures the spectrum tail shift towards small scales. The associated spatial fields have been presented in Figure (2).

As simplified, the initial spectrum tail can then be recovered using an isotropic Gaussian filtering of the tracer with a degree of smoothness controlled by the variance coefficient:

$$\frac{\|T_0\|^2}{\|\nabla T_0\|^2} \frac{1}{1 + (\frac{\tau_G}{t})^2}. \quad (3.21)$$

This adaptive filtering is exemplified in Figure 13. The tracer is advected during a time t , and then smoothens by a Gaussian filter with the width (3.21). The combine effect of advection and filtering moves the large-scale structures, but keeps the global amount of small-scale structures stationary.

3.4 Self-similar approximation

Even though the previous Gaussian approximation is useful to link advection and filtering, spectra of geo-physical tracer field are more likely self-similar, and possibly non-smooth. Moreover, it can be useful to target specific spectral slopes using the Lagrangian advection method. For these reasons, we consider the following form for the spectrum of a scalar f :

$$\bar{\Gamma}_f(\kappa) = \begin{cases} A \left(1 + \frac{\kappa}{\kappa_m}\right)^{-\zeta} & \text{if } \kappa \leq \kappa_\infty \\ 0 & \text{otherwise} \end{cases}, \quad (3.22)$$

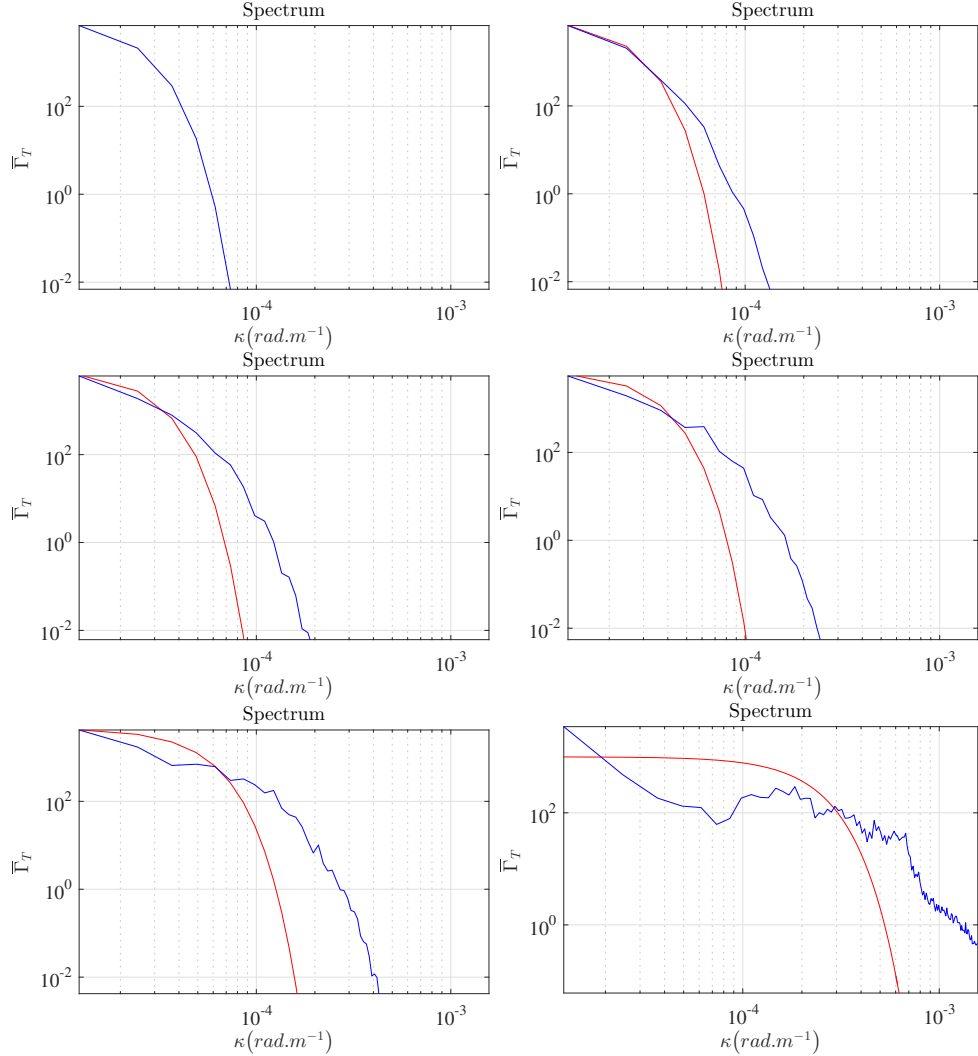


Figure 12: Omnidirectional spectra (blue) and its prediction using the Gaussian approximation (3.20) (red) for the toy model at $t = 0, 5, 10, 15, 30$ and 150 days. The associated spatial fields are displayed in Figure 2.

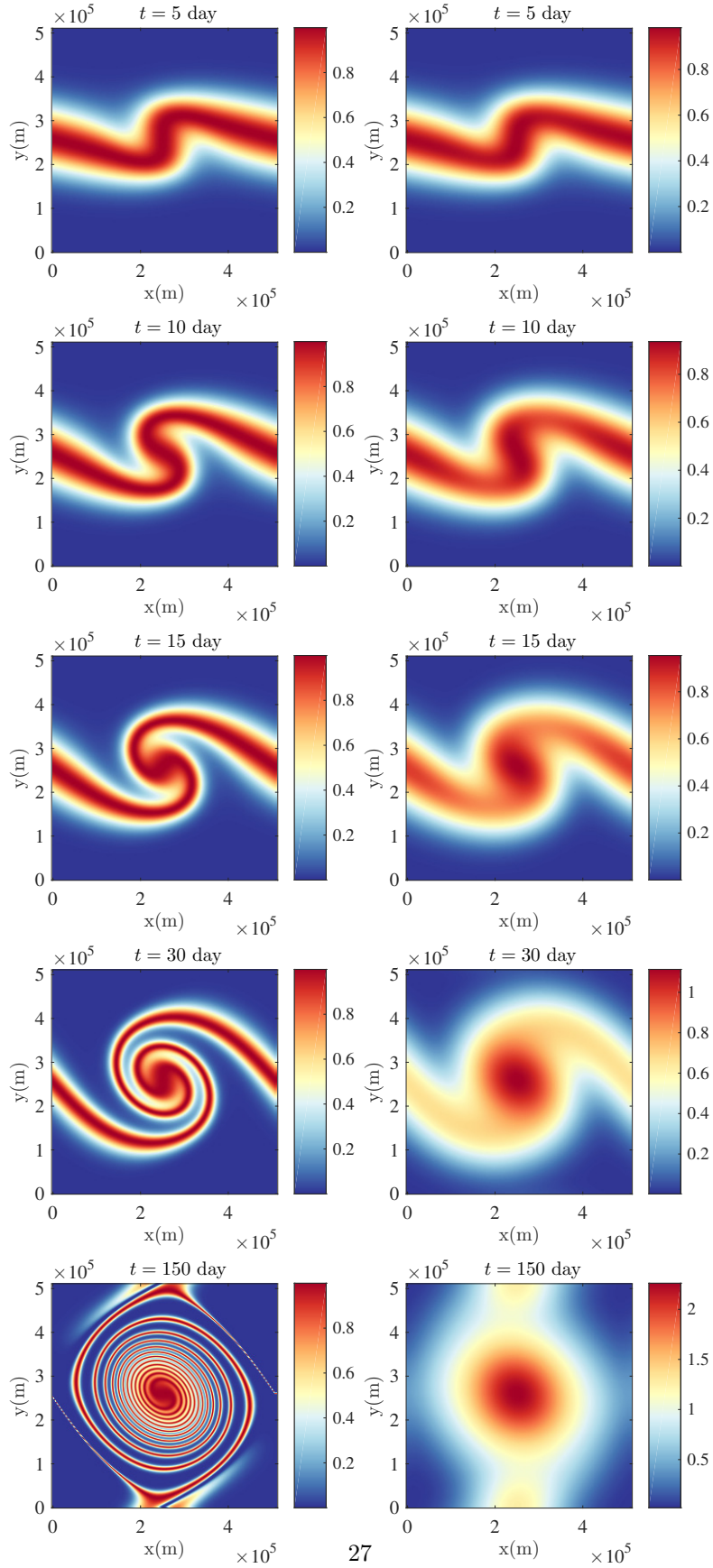


Figure 13: Tracer advected (left) and tracer advected and then smoothed by our adapted Gaussian filter (right) for the toy model at (from top to bottom) $t = 5, 10, 15, 30$ and 150 days.

Then,

$$L_f^2 = \frac{\|f\|^2}{\|\nabla f\|^2}, \quad (3.23)$$

$$= \frac{\int_0^{\kappa_\infty} \left(1 + \frac{\kappa}{\kappa_m}\right)^{-\zeta}}{\int_0^{\kappa_\infty} \kappa^2 \left(1 + \frac{\kappa}{\kappa_m}\right)^{-\zeta}}, \quad (3.24)$$

$$= \frac{(\zeta - 2)(\zeta - 3)}{\kappa_m^2 \left(2 - \left(1 + \frac{\kappa_\infty}{\kappa_m}\right)^{1-\zeta} \left((\zeta - 1)(\zeta - 2) \left(\frac{\kappa_\infty}{\kappa_m}\right)^2 + 2(\zeta - 1)\frac{\kappa_\infty}{\kappa_m} + 2\right)\right)}. \quad (3.25)$$

where κ_∞ is set by the numerical resolution. As long as the width of the inertial scale, $\kappa_\infty - \kappa_m$, is large enough, the above function is strictly positive and continuous w.r.t. the spectral slope, ζ , for all $\zeta > 1$.

For $f = T$ being the advected tracer, the wavenumber κ_m can encompass planetary length scales which does not vary much during the process of advection. This weak variation is due to the spatial correlation between tracer and flow (see (2.13)), but also to the relatively small advection time (mesoscale or submesoscale time scales). The resolution, κ_∞ , is constant as well. So, a targeted spectral slope, ζ , provides a length scale L_f to be reached on a given advection time, making use of (3.21).

Figure 14 illustrates this estimate, applied to the ACC SST field presented in the last section. As prescribed by the model, the spectrum tail slope of the advected SST reaches the value -3 after 5 days of advection, 2.5 after 10 days and -2 after 48 days. Figure 9 displays the spatial SST fields before and after advection. These data correspond to the summer (January in the southern hemisphere).

Interestingly, the seasonality variation can be studied. Figure 15 displays, for each day of the year 2011, the global stretching time, τ_G , the spectrum slope of the measured SST and the prescribed advection time to reach a -2.5 spectrum slope. As found, the stretching is faster during the winter, likely associated with a more intense eddy activity. The measured SST spectral slopes are relatively stationary (close to -4), whereas the small-scale velocity is expected to be stronger during winter. Accordingly, the prescribed advection time is smaller in wintertime.

Berti and Lapeyre (2014) proposed other Eulerian means to prescribe the advection time: the inverse of the vorticity Root Mean Square (RMS), $\left(\overline{(\nabla^\perp \cdot \mathbf{v})^2}\right)^{-1/2}$, and of the velocity gradient RMS, $\left(\overline{\|\nabla \mathbf{v}\|^2}\right)^{-1/2}$. The latter is directly linked to the shearing time (2.34). Yet, these estimates can encode shearing but not folding. Indeed, folding involves 2^{nd} order derivatives of the velocity, such as to describe the curvature variation of adjacent streamlines (2.53). Moreover, these criteria do not depend on the initial nor on the resulting spectral slope. So, these criteria cannot fully control the necessary advection time, and shall likely lead to wrong resulting tracer spectral slopes. For instance, Figure 15 demonstrates that these criteria strongly underestimate the advection time needed to reach a -2.5 spectrum slope. Accordingly, these criteria mostly apply to very short advection time, with a resulting advected tracer already close to the true SST.

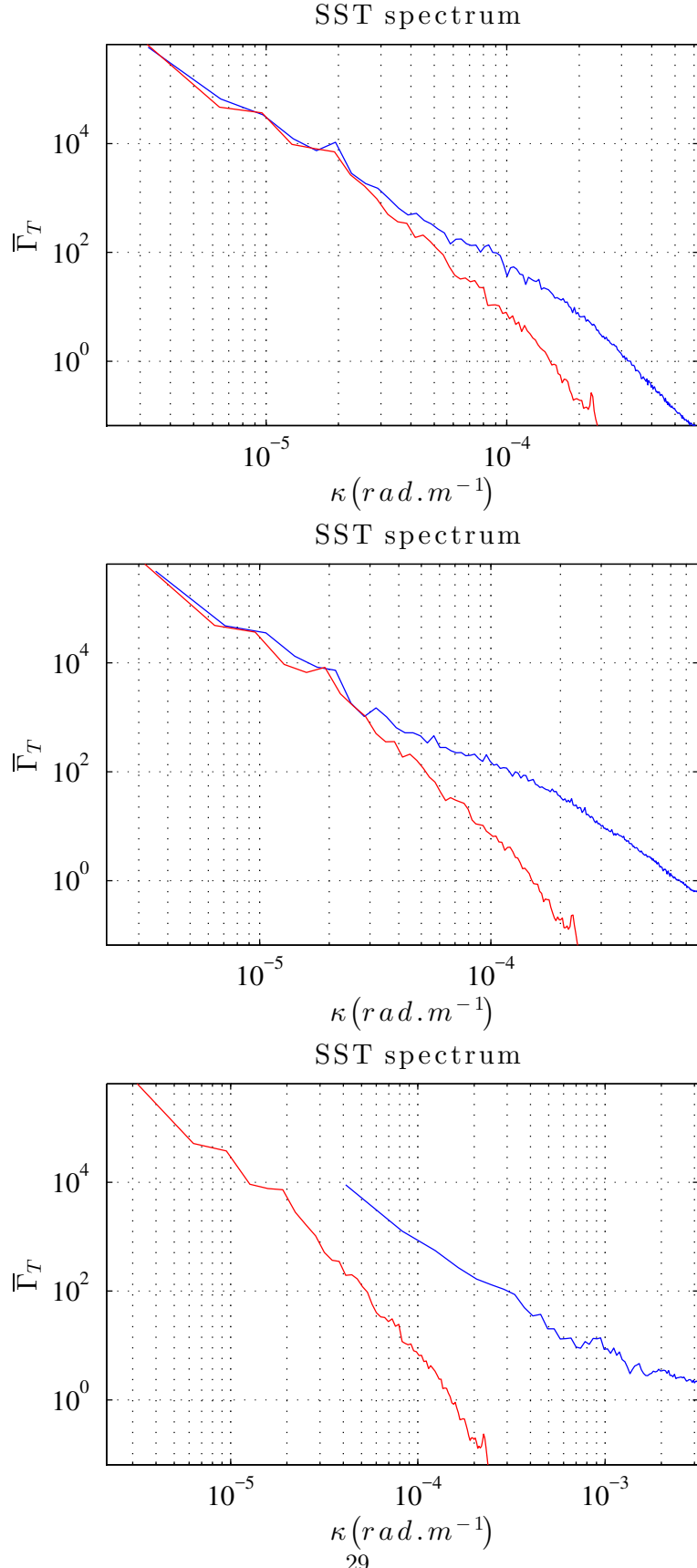


Figure 14: SST spectrum of the satellite data (red) and after prescribed advection (blue) with 5 days for a -3 spectrum slope (top), 10 days for a -2.5 spectrum slope (middle) and 48 days for a -2 spectrum slope (bottom). The associated spatial fields are presented in Figure 9. On the blue bottom spectrum, missing large-scale values are due to a strong deformation of the advected spatial domain by the jet (see Figure 9).

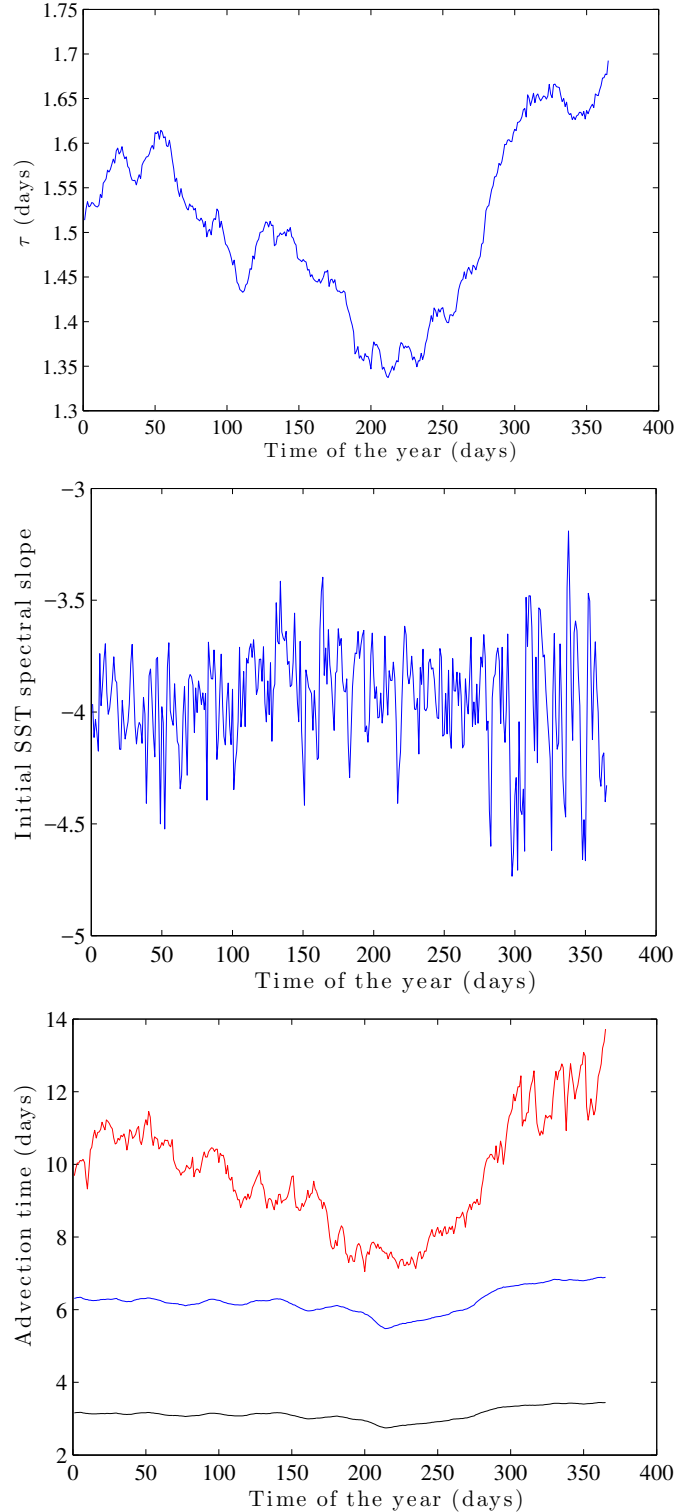


Figure 15: Global stretching time, τ_G (top in days), SST spectrum slope of Globcurrent data (middle) and prescribed advection time to reach a -2.5 spectrum slope (bottom in days) with the velocity gradient RMS (blue line), vorticity RMS (black line) and our model (red line).

4 Estimation of eddy diffusivity

Considering satellite observations, geophysical tracers generally exhibit relatively stable spectra. The predicted raise of the tracer spectral tail, under multiple advection operations, shall thus be compensated. This can possibly be resulting from the combined effects of the well resolved, slow-varying and large-scale, velocity, and of an unresolved, fast-varying and likely small-scale, velocity. As the first velocity component will tend to raise the spectrum (3.20), the second component shall act to the mean tracer. As often suggested, this last process can be accounted for using a uniform eddy diffusivity, ν . As such, after an advection of Δt , it multiplies the spectrum by $\exp(-\nu\Delta t\kappa^2)$. To exactly compensate the spectrum increase (3.20) during Δt , and thus to keep the resulting advected tracer closer to its initial variance distribution over scales, the eddy diffusivity can then be set as:

$$\nu = \frac{1}{2\tau_G} \frac{\|T_0\|^2}{\|\nabla T_0\|^2} c(t) \quad \text{with} \quad c(t) = \frac{\frac{\Delta t}{\tau_G}}{\left(1 + \left(\frac{\Delta t}{\tau_G}\right)^2\right)} = \begin{cases} \frac{\Delta t}{\tau_G} & \text{if } \Delta t \ll \tau_G \\ \frac{\tau_G}{\Delta t} & \text{if } \Delta t \gg \tau_G \end{cases}. \quad (4.1)$$

For small time step, Δt , the eddy diffusivity is superdiffusive, whereas for large time step it is subdiffusive. Note also that in the second case, the direct cascade intensifies, decreasing the large-scale tracer energy as encoded by the multiplicative constant of (3.20):

$$\left(\frac{\|\nabla T_0\|^2}{\|\nabla T\|^2}\right)^{1/2} \approx \left(1 + \left(\frac{\Delta t}{\tau_G}\right)^2\right)^{-1/2} = \begin{cases} 1 & \text{if } \Delta t \ll \tau_G \\ \frac{\tau_G}{\Delta t} & \text{if } \Delta t \gg \tau_G \end{cases}. \quad (4.2)$$

Conclusion

Through this chapter, we analyzed how sets of points are stretched and folded by a smooth, possibly stationary, flow, creating strong tracer gradients and raising the spectral tail of the initial tracer spectral distribution.

Two characteristics of the flow influence the norm of advected tracer gradients: a local growth rate, associated with the eigenvalues of the Cauchy-Green tensor, and the orientation of the stable direction, eigenvector of the Cauchy-Green tensor. Integrated over space, the influence of local orientation disappears if the initial tracer is not correlated to the flow. The overall gradients can then only strengthen. Such a weak correlation applies for passive tracers, having negligible back effects on the flow, but such a weak correlation can also appear when the tracer is strongly smoothed before being advected. The growth rate can then be readily related to FTLE and mesochronic velocity. If the Eulerian velocity is stationary, the gradient strengthening is mainly due to locally uniform shears and stationary convective cells. The first process stretches pairs of points when the streamlines are straights and parallel. The second one folds and wraps the tracer around vortices. Indeed, different concentric orbits are associated with different temporal periods. A local, in space, temporal frequency can then be understood as an angular velocity, and its spatial variations deform the tracer structures. For both the velocity shears and angular velocity shears, the norm of tracer gradients linearly increases in time. Integrated over space, the square of this norm controls and specifies the time

evolution of the tracer correlation length, the spectral tail and its slope. Two simplified models are proposed to approximate the tracer spectrum tail. These models only depend on the advection time, the Eulerian velocity and the initial tracer statistical characteristics. Numerical simulations on a toy model and real satellite images confirm the validity of these different approximations. In particular, we successfully estimate the spatial and spectral distribution, as well as the time evolution of the mixing processes. We apply the method to specify the advection time and the filter width of the Lagrangian advection method. Moreover, the proposed development can help the definition of an eddy diffusion coefficient as a function of the large-scale velocity. Finally, this work highlights the preponderant effect of folding in finite-time mixing.

References

- H. Aref. Stirring by chaotic advection. *Journal of fluid mechanics*, 143:1–21, 1984.
- S. Berti and G. Lapeyre. Lagrangian reconstructions of temperature and velocity in a model of surface ocean turbulence. *Ocean Modelling*, 76:59–71, 2014.
- M. Budišić and J.-L. Thiffeault. Finite-time braiding exponents. *Chaos: An Interdisciplinary Journal of Nonlinear Science*, 25(8):087407, 2015.
- G. Dencausse, R. Morrow, M. Rogé, and S. Fleury. Lateral stirring of large-scale tracer fields by altimetry. *Ocean Dynamics*, 64(1):61–78, 2014.
- F. d’Ovidio, J. Isern-Fontanet, C. López, E. Hernández-García, and E. García-Ladona. Comparison between eulerian diagnostics and finite-size Lyapunov exponents computed from altimetry in the algerian basin. *Deep Sea Research Part I: Oceanographic Research Papers*, 56(1):15–31, 2009.
- C. Dufau, M. Orsztynowicz, G. Dibarboure, R. Morrow, and P.-Y. Le Traon. Mesoscale resolution capability of altimetry: Present and future. *Journal of Geophysical Research: Oceans*, 2016.
- G. Falkovich, K. Gawędzki, and M. Vergassola. Particles and fields in fluid turbulence. *Reviews of modern Physics*, 73(4):913, 2001.
- J. Gower, K. Denman, and R. Holyer. Phytoplankton patchiness indicates the fluctuation spectrum of mesoscale oceanic structure. *Nature*, 288:157–159, 1980.
- G. Haller. An objective definition of a vortex. *Journal of fluid mechanics*, 525:1–26, 2005.
- G. Haller and T. Sapsis. Lagrangian coherent structures and the smallest finite-time Lyapunov exponent. *Chaos: An Interdisciplinary Journal of Nonlinear Science*, 21(2):023115, 2011.
- G. Haller and G. Yuan. Lagrangian coherent structures and mixing in two-dimensional turbulence. *Physica D: Nonlinear Phenomena*, 147(3):352–370, 2000.
- Y. Lehahn, F. d’Ovidio, M. Lévy, and E. Heifetz. Stirring of the northeast atlantic spring bloom: A Lagrangian analysis based on multisatellite data. *Journal of Geophysical Research: Oceans*, 112(C8), 2007.

- M. Lesieur and R. Sardouny. Satellite-sensed turbulent ocean structure. *Nature*, 294:673, 1981.
- T. Ma, N. Ouellette, and E. Boltt. Stretching and folding in finite time. *Chaos: An Interdisciplinary Journal of Nonlinear Science*, 26(2):023112, 2016.
- I. Mezić, S. Loire, V. Fonoferov, and P. Hogan. A new mixing diagnostic and gulf oil spill movement. *Science*, 330(6003):486–489, 2010.
- A. Okubo. Horizontal dispersion of floatable particles in the vicinity of velocity singularities such as convergences. 17(3):445–454, 1970.
- R. Pierrehumbert and H. Yang. Global chaotic mixing on isentropic surfaces. *Journal of the atmospheric sciences*, 50(15):2462–2480, 1993.
- J. Price, M. Reed, M. Howard, W. Johnson, Z.-G. Ji, C. Marshall, N. Guinasso, and G. Rainey. Preliminary assessment of an oil-spill trajectory model using satellite-tracked, oil-spill-simulating drifters. *Environmental Modelling & Software*, 21(2):258–270, 2006.
- B. Shivamoggi and G. van Heijst. The Okubo-Weiss criteria in two-dimensional hydrodynamic and magnetohydrodynamic flows. *arXiv preprint arXiv:1110.6190*, 2011.
- J.-L. Thiffeault. Stretching and curvature of material lines in chaotic flows. *Physica D: Nonlinear Phenomena*, 198(3):169–181, 2004.
- J.-L. Thiffeault and A. Boozer. Geometrical constraints on finite-time Lyapunov exponents in two and three dimensions. *Chaos: An Interdisciplinary Journal of Nonlinear Science*, 11(1):16–28, 2001.
- G. Vallis. *Atmospheric and oceanic fluid dynamics: fundamentals and large-scale circulation*. Cambridge University Press, 2006.
- J. Weiss. The dynamics of enstrophy transfer in two-dimensional hydrodynamics. *Physica D: Nonlinear Phenomena*, 48(2):273–294, 1991.
- P. Welander. Studies on the general development of motion in a two-dimensional, ideal fluid. *Tellus*, 7(2):141–156, 1955.

A Omnidirectional spectra of tracers for smooth flow

Hereafter, we will focus on the omnidirectional spectrum of a scalar f . This will enable us to replace $\nabla f(\nabla f)^T$ by $\|\nabla f(\mathbf{x})\|^2$ in the expression of the spectrum (3.13).

$$\begin{aligned}
\bar{\Gamma}_f(\kappa) &= \kappa \oint_{[0,2\pi]} d\theta_k \Gamma_f(k), \\
&= \kappa \oint_{[0,2\pi]} d\theta_k \int_{\Omega} d\delta x \gamma_f(\delta x) e^{-ik \cdot \delta x}, \\
&= \kappa \oint_{[0,2\pi]} d\theta_k \int_{\Omega} d\delta x \left(\gamma_f(0) - \frac{1}{2} \delta x^T \frac{1}{S} \mathbb{E} \int_{\Omega} dx \nabla f(x) (\nabla f(x))^T \delta x + \underset{\|\delta x\| \rightarrow 0}{O}(\|\delta x\|^3) \right) e^{-ik \cdot \delta x}, \\
&= \frac{\kappa}{S} \mathbb{E} \oint_{[0,2\pi]} d\theta_k \int_{\Omega} d\delta x \int_{\Omega} dx \left(f^2(x) - \frac{1}{2} \delta x^T \nabla f(x) (\nabla f(x))^T \delta x + \underset{\|\delta x\| \rightarrow 0}{O}(\|\delta x\|^3) \right) e^{-ik \cdot \delta x}, \\
&= \frac{\kappa}{S} \mathbb{E} \int_{\Omega} dx \oint_{[0,2\pi]} d\theta_k \int_{\Omega} d\delta x \left(f^2(x) - \frac{1}{2} \left(\frac{\nabla f(x)}{\|\nabla f(x)\|_2} \cdot \delta x \right)^2 \|\nabla f(x)\|_2^2 + \underset{\|\delta x\| \rightarrow 0}{O}(\|\delta x\|^3) \right) e^{-ik \cdot \delta x}.
\end{aligned}$$

Locally in \mathbf{x} , we can define a variable change for $\delta x = (\delta x_1 \ \delta x_2)^T$. We apply the rotation matrix $\mathbf{U}(\mathbf{x}) = \frac{1}{\|\nabla f(\mathbf{x})\|_2} [\nabla f(\mathbf{x}) \ \nabla^\perp f(\mathbf{x})]$ to δx to align δx with the tracer gradient and denote $\theta(\mathbf{x})$ the angle of the associated rotation:

$$\begin{aligned}
\bar{\Gamma}_f(\kappa) &= \frac{\kappa}{S} \mathbb{E} \int_{\Omega} dx \oint_{[0,2\pi]} d\theta_k \int_{\Omega} d\delta x \left(f^2(\mathbf{x}) - \frac{1}{2} (\delta x_1)^2 \|\nabla f(\mathbf{x})\|_2^2 + \underset{\|\delta x\| \rightarrow 0}{O}(\|\delta x\|^3) \right) e^{-i(\mathbf{U}^T k) \cdot \delta x}, \\
&= \frac{\kappa}{S} \mathbb{E} \int_{\Omega} dx \oint_{[\theta(\mathbf{x}), \theta(\mathbf{x})+2\pi]} d\theta_k \int_{\Omega} d\delta x \left(f^2(\mathbf{x}) - \frac{1}{2} (\delta x_1)^2 \|\nabla f(\mathbf{x})\|_2^2 + \underset{\|\delta x\| \rightarrow 0}{O}(\|\delta x\|^3) \right) e^{-ik \cdot \delta x}, \\
&= \frac{\kappa}{S} \mathbb{E} \int_{\Omega} dx \oint_{[0,2\pi]} d\theta_k \int_{\Omega} d\delta x \left(f^2(\mathbf{x}) - \frac{1}{2} (\delta x_1)^2 \|\nabla f(\mathbf{x})\|_2^2 + \underset{\|\delta x\| \rightarrow 0}{O}(\|\delta x\|^3) \right) e^{-ik \cdot \delta x}, \\
&= \kappa \oint_{[0,2\pi]} d\theta_k \int_{\Omega} d\delta x \left(\overline{\|f\|^2} - \frac{1}{2} (\delta x_1)^2 \overline{\|\nabla f\|^2} + \underset{\|\delta x\| \rightarrow 0}{O}(\|\delta x\|^3) \right) e^{-ik \cdot \delta x}.
\end{aligned}$$

The third equality above is due to the averaging over the spatial frequency angle θ_k . Indeed, $\mathbf{U}^T k$ is just a rotation of k . And, integrating over $[0, 2\pi]$ or over $[\theta(\mathbf{x}), 2\pi + \theta(\mathbf{x})]$ is the same thing, since it leads to the same closed line: a circle of radius κ .

$$\begin{aligned}
\bar{\Gamma}_f(\kappa) &= \kappa \oint_{[0,2\pi]} d\theta_k \int_{\Omega} d\delta x_1 d\delta x_2 \left(\overline{\|f\|^2} \exp \left(-\frac{1}{2} \frac{\overline{\|\nabla f\|^2}}{\overline{\|f\|^2}} (\delta x_1)^2 \right) + \underset{\|\delta x\| \rightarrow 0}{O}(\|\delta x\|^3) \right) \\
&\quad \times e^{-ik_1 \delta x_1} e^{-ik_2 \delta x_2}, \\
&\underset{\|\mathbf{k}\| \rightarrow \infty}{\sim} \oint_{[0,2\pi]} \kappa d\theta_k \frac{C_f}{2(2\pi)} \exp \left(-\frac{1}{2} L_f^2 k_1^2 \right) (2\pi) \delta(k_2),
\end{aligned}$$

where $\mathbf{k} = \begin{pmatrix} k_1 \\ k_2 \end{pmatrix} = \begin{pmatrix} \kappa \cos(\theta_k) \\ \kappa \sin(\theta_k) \end{pmatrix}$, $L_f^2 = \frac{\overline{\|f\|^2}}{\overline{\|\nabla f\|^2}}$ and $\frac{C_f}{2(2\pi)} = \left(\frac{2\pi(\overline{\|f\|^2})^3}{\overline{\|\nabla f\|^2}} \right)^{1/2}$. Note that the asymptotic equivalence is an approximation. Then, switching from cylindrical to Cartesian coordinates in each half ring

$\{\mathbf{k} \in \mathbb{R}^2 | k_1 \leq 0, \|\mathbf{k}\| = \kappa\}$ and $\{\mathbf{k} \in \mathbb{R}^2 | k_1 \geq 0, \|\mathbf{k}\| = \kappa\}$ yields:

$$\begin{aligned}\bar{\Gamma}_f(\kappa) &\underset{\|\mathbf{k}\| \rightarrow \infty}{\sim} 2 \int_{-\kappa}^{\kappa} \frac{dk_2}{\sqrt{1 - \left(\frac{k_2}{\kappa}\right)^2}} \frac{C_f}{2} \exp\left(-\frac{1}{2} L_f^2 (\kappa^2 - k_2^2)\right) \delta(k_2), \\ &\underset{\|\mathbf{k}\| \rightarrow \infty}{\sim} C_f \exp\left(-\frac{1}{2} L_f^2 \kappa^2\right).\end{aligned}$$